

---

This is an electronic reprint of the original article.  
This reprint may differ from the original in pagination and typographic detail.

Baghel, Janhavi; Kharb, P.; Hovatta, T.; Ho, Luis C.; Harrison, C.; Lindfors, E.; Silpa, S.; Gulati, S.

## Investigating Differences in the Palomar-Green Blazar Population Using Polarization

*Published in:*  
Astrophysical Journal

*DOI:*  
[10.3847/1538-4357/ad8d58](https://doi.org/10.3847/1538-4357/ad8d58)

Published: 01/12/2024

*Document Version*  
Publisher's PDF, also known as Version of record

*Published under the following license:*  
CC BY

*Please cite the original version:*  
Baghel, J., Kharb, P., Hovatta, T., Ho, L. C., Harrison, C., Lindfors, E., Silpa, S., & Gulati, S. (2024). Investigating Differences in the Palomar-Green Blazar Population Using Polarization. *Astrophysical Journal*, 977(2), Article 192. <https://doi.org/10.3847/1538-4357/ad8d58>

---

This material is protected by copyright and other intellectual property rights, and duplication or sale of all or part of any of the repository collections is not permitted, except that material may be duplicated by you for your research use or educational purposes in electronic or print form. You must obtain permission for any other use. Electronic or print copies may not be offered, whether for sale or otherwise to anyone who is not an authorised user.



# Investigating Differences in the Palomar-Green Blazar Population Using Polarization

Janhavi Baghel<sup>1</sup> , P. Kharb<sup>1</sup> , T. Hovatta<sup>2,3</sup> , Luis C. Ho<sup>4,5</sup> , C. Harrison<sup>6</sup> , E. Lindfors<sup>2</sup>, Silpa S.<sup>7</sup> , and S. Gulati<sup>1</sup> <sup>1</sup> National Centre for Radio Astrophysics (NCRA)—Tata Institute of Fundamental Research (TIFR), S. P. Pune University Campus, Ganeshkhind, Pune 411007, India; [jbaghel@ncra.tifr.res.in](mailto:jbaghel@ncra.tifr.res.in)<sup>2</sup> Finnish Centre for Astronomy with ESO, FINCA, University of Turku, Turku, Finland<sup>3</sup> Aalto University Metsähovi Radio Observatory, Metsähovintie 114, 02540 Kylmälä, Finland<sup>4</sup> Kavli Institute for Astronomy and Astrophysics, Peking University, Beijing 100871, People's Republic of China<sup>5</sup> Department of Astronomy, School of Physics, Peking University, Beijing 100871, People's Republic of China<sup>6</sup> School of Mathematics, Statistics and Physics, Newcastle University, Newcastle upon Tyne NE1 7RU, UK<sup>7</sup> Departamento de Astronomía, Universidad de Concepción, Barrio Universitario s/n, Concepción, Chile

Received 2024 July 18; revised 2024 October 15; accepted 2024 October 29; published 2024 December 12

## Abstract

We present polarization images with the Karl G. Jansky Very Large Array (VLA) in A- and B-array configurations at 6 GHz of seven radio-loud (RL) quasars and eight BL Lac objects belonging to the Palomar-Green (PG) “blazar” sample. This completes our arcsecond-scale polarization study of an optically selected volume-limited blazar sample comprising 16 radio-loud quasars and 8 BL Lac objects. Using the VLA, we identify kiloparsec-scale polarization in the cores and jets/lobes of all the blazars, with fractional polarization varying from around  $0.8\% \pm 0.3\%$  to  $37\% \pm 6\%$ . The kiloparsec-scale jets in PG RL quasars are typically aligned along their parsec-scale jets and show apparent magnetic fields parallel to jet directions in their jets/cores and magnetic field compression in their hot spots. The quasars show evidence of interaction with their environment as well as restarted active galactic nucleus activity through morphology, polarization, and spectral indices. These quasi-periodic jet modulations and restarted activity may be indicative of an unstable accretion disk undergoing transition. We find that the polarization characteristics of the BL Lacs are consistent with their jets being reoriented multiple times, with no correlation between their core apparent magnetic field orientations and parsec-scale jet directions. We find that the low synchrotron peaked BL Lacs show polarization and radio morphology features typical of “strong” jet sources as defined by E. T. Meyer et al. for the “blazar envelope scenario,” which posits a division based on jet profiles and velocity gradients rather than total jet power.

*Unified Astronomy Thesaurus concepts:* Active galaxies (17); Blazars (164); BL Lacertae objects (158); Quasars (1319); Radio jets (1347); Polarimetry (1278)

## 1. Introduction

Active galactic nuclei (AGN) are highly energetic phenomena produced by the central supermassive black hole of a galaxy devouring the inflowing gas and dust (M. J. Rees 1984; S. Rawlings & R. Saunders 1991). This spiraling debris forms a rotating accretion disk that emits intense radiation due to frictional heating (D. Lynden-Bell 1969; J. M. Bardeen 1970). A fraction of these AGN also expel relativistic jets of synchrotron-emitting plasma orthogonal to the accretion disks and are bright at radio frequencies (R. D. Blandford & M. J. Rees 1974). Radio-loud (RL) AGN have strong, large-scale jets and are defined as having their 5 GHz radio flux density at least 10 times greater than their optical *B*-band flux densities (K. I. Kellermann et al. 1989). These jets have the potential to significantly influence their host galaxy and surrounding environment, as they heat the intracluster medium (B. R. McNamara & P. E. J. Nulsen 2007; P. Chang et al. 2012) and modulate star formation rates (A. Cattaneo et al. 2009; J. Shin et al. 2019).

There are many observational subclassifications of RL AGN, and most can be explained through differences in viewing angles and beaming (M. J. Rees 1966; A. C. S. Readhead et al. 1978). However, some delineations are independent of orientation. One

such dichotomy is based on the appearance of two distinctive radio jet morphologies—Fanaroff and Riley type I and II (FRI and FRII; B. L. Fanaroff & J. M. Riley 1974). The FRI jets are fainter, diffuse plumes whereas the FRII jets are brighter, highly collimated, and produce terminal hot spots when they impact the ambient medium (R. D. Blandford & M. J. Rees 1974; B. Mingo et al. 2019).

The underlying cause of the FR dichotomy continues to be a subject of much debate as is its initial correlation with the extended radio luminosity and, subsequently, jet power (E. G. Blackman & S. V. Lebedev 2022). Potential explanations can be broadly categorized into intrinsic factors relating to differences in jet kinetic power arising from differences in black hole spins (S. A. Baum et al. 1995; D. L. Meier 1999), accretion modes (P. N. Best & T. M. Heckman 2012; M. Hardcastle 2018), jet formation mechanisms (R. D. Blandford & R. L. Znajek 1977; R. D. Blandford & D. G. Payne 1982), or jet profile and particle compositions (P. A. G. Scheuer 1974; R. A. Laing & A. H. Bridle 2002; J. H. Croston et al. 2018), and extrinsic factors relating to jet–medium interaction such as jet decollimation due to turbulence-induced plasma flow instabilities (G. V. Bicknell 1984; R. A. Laing & A. H. Bridle 2002) and stellar mass loading (S. S. Komissarov 1994; S. Wykes et al. 2015) or the fast deceleration of an initially supersonic jet due to interaction with a denser ambient medium (J. A. Biretta et al. 1995; M. J. Hardcastle et al. 2003).

As per the radio-loud unification scheme (C. M. Urry & P. Padovani 1995), RL quasars are the pole-on counterparts of



Original content from this work may be used under the terms of the [Creative Commons Attribution 4.0 licence](https://creativecommons.org/licenses/by/4.0/). Any further distribution of this work must maintain attribution to the author(s) and the title of the work, journal citation and DOI.

FRII radio galaxies, and BL Lac objects are the pole-on counterparts of FRI radio galaxies. Collectively referred to as blazars, their jets are at small angles to our line of sight. Blazars were originally differentiated based on their optical spectra. BL Lacs have weak optical line emission compared to quasars, which are characterized by stronger optical line emission (equivalent widths  $>5 \text{ \AA}$ ; M. Stickel et al. 1991; J. T. Stocke et al. 1991). Given their high beaming and strong variability and no evidence of differences in beaming among the two classes, the BL Lacs are thought to be at similar angles to the flat-spectrum radio quasars (FSRQs; G. Ghisellini et al. 1993; D. C. Gabuzda et al. 2000). The steep-spectrum radio quasars (SSRQs) and FSRQs both display broad (velocity widths  $\geq 1000 \text{ km s}^{-1}$ ) emission lines in their optical/UV spectra. Given that the half-opening angle of the dusty obscuring tori is  $\leq 50^\circ$  (C. Simpson et al. 1996), their jets are assumed to be inclined at angles  $\leq 50^\circ$  to our lines of sight. The SSRQs and FSRQs are therefore progressively more aligned versions of FRII galaxies (P. D. Barthel 1989). BL Lacs are also characterized by systematically lower apparent jet speeds compared to FSRQs at parsec scales (G. Ghisellini et al. 1993; D. C. Gabuzda et al. 2000; K. I. Kellermann et al. 2004), which given their similar orientations suggests a difference in the actual intrinsic velocities of relativistic bulk motion.

With polarimetric Very Long Baseline Interferometry (VLBI) observations, differences in the apparent magnetic (B) fields among the parsec-scale jets of the two blazar classes have been found (D. C. Gabuzda et al. 1992; T. V. Cawthorne et al. 1993). BL Lacs tend to have their parsec-scale electric vector position angle (EVPA) parallel to the jet direction, whereas RL quasars tend to show a perpendicular relative orientation (M. L. Lister & D. C. Homan 2005; M. L. Lister et al. 2013). The inferred B-field structures are perpendicular to the EVPAs for optically thin<sup>8</sup> emission (A. G. Pacholczyk 1970), so this would mean that the BL Lacs show a predominance of jet B fields orthogonal to the jet direction while quasars primarily show jet B fields along the jet direction. One explanation for such a B-field structure could be the tightness or looseness of the helical magnetic fields in BL Lacs and quasars, respectively (e.g., D. C. Gabuzda 2015).

Blazars are also subcategorized based on their spectral energy distributions (SEDs) into high-, intermediate-, and low-spectrally peaked based on the position of their synchrotron peak frequency (A. A. Abdo et al. 2010; P. Padovani & P. Giommi 2015). Contradicting the notion of the FR dichotomy, several studies have found a broad continuum in parameters such as synchrotron peak frequencies and spectral indices (P. Giommi & P. Padovani 1994; R. M. Sambruna et al. 1996). Notably, G. Fossati et al. (1998) found an anticorrelation between the luminosity and frequency of the synchrotron peak. This anticorrelation, now referred to as the “blazar sequence,” implies that the total jet power is the only parameter informing the spectral type and broadband SED characteristics of an AGN. Later studies by G. Ghisellini et al. (2017) found the sequence to exist for the BL Lac objects but not for the quasars, which was interpreted as a sequence of radiative cooling due to the presence of the broad-line region (BLR) and the dusty torus in the case of quasars.

More recent work by E. T. Meyer et al. (2011) and M. Keenan et al. (2021) have given rise to the “blazar envelope” picture. Under this scenario, a range of progressively misaligned but intrinsically different “weak” and “strong” jets are hosted by sources with inefficient accretion and low-excitation spectral lines or efficient accretion and high-excitation spectral lines, respectively. The FRII radio galaxies and quasars have “strong” jets and so do low-synchrotron-peaked (LSP) BL Lacs, whereas FRI radio galaxies and high-synchrotron-peaked (HSP) BL Lacs have “weak” jets with intermediate-synchrotron-peaked (ISP) BL Lacs coming from a mixed population. Low to moderately high jet power is generated by either type of jet but extreme high-power jets are exclusively “strong” jet sources.

Given that high- and low-excitation radio galaxies both exhibit FRI and FRII morphologies (P. N. Best & T. M. Heckman 2012; B. Mingo et al. 2022) and the fact that hybrid morphology sources exist, it implies that the environment may play a larger role in determining the radio morphology. Beaming and light travel time differences between the two lobes may also cause an intrinsically FRII source to look like a hybrid source (Gopal-Krishna et al. 1996; P. Kharb et al. 2015; J. J. Harwood et al. 2020; S. Ghosh et al. 2023).

Given the complexity of these classifications and their interrelated nature, we aimed to disentangle the base causes of these differences in jet profiles. Since FRI jets decelerate and decollimate on kiloparsec scales (G. V. Bicknell 1994; R. A. Laing & A. H. Bridle 2002) and magnetic fields play a critical role in bulk acceleration and jet propagation (D. L. Meier et al. 2001; J. F. Hawley et al. 2015), kiloparsec-scale radio polarimetric observations form an important means of investigating the differences in jet characteristics. Blazars with their higher total and polarized flux densities form ideal candidates to investigate the FR dichotomy as well as the blazar divide.

With this in mind, we set out to investigate the differences in blazars using kiloparsec-scale polarization with the upgraded Giant Metrewave Radio Telescope (uGMRT) and the Karl G. Jansky Very Large Array (VLA). Our objective was to investigate whether the differences in polarization among the blazar subclasses at the parsec scale persist until the kiloparsec scale. We also aim to increase the number of high-sensitivity kiloparsec-scale images of BL Lacs, which are currently in short supply compared to quasars (M. Giroletti et al. 2006).

This paper is a continuation of our study of the Palomar-Green (PG) sample (R. F. Green et al. 1986) of blazars (J. Baghel et al. 2023; J. Baghel et al. 2024). Results from uGMRT Band-4 (650 MHz) data for the PG BL Lac objects were presented in J. Baghel et al. (2024), while VLA C-band (6 GHz) B-array data for 9 out of 16 quasars was presented in J. Baghel et al. (2023). In this paper, we present the VLA polarization images for the remaining RL quasars and all BL Lac objects (see Table 1) to study the kiloparsec-scale B-field structures of the entire PG “blazar” sample.

The sample selection is discussed briefly in Section 2. The radio data reduction and calibration and imaging details are presented in Section 3. Our observational results are discussed in Section 4 along with a brief discussion on existing literature on the sources. In Section 5 we present the global correlations for the entire PG “blazar” sample. Section 6 discusses our findings, and Section 7 provides our conclusions.

<sup>8</sup> The optical thickness required to change the inference of B-field direction is considered to be  $\tau \sim 7$  (T. V. Cawthorne & P. A. Hughes 2013; J. Wardle 2018).

**Table 1**  
The Subset of PG “Blazar” Sample Presented in This Paper

S.No.	Name	Other Name	R.A.	Decl.	Redshift <sup>a</sup>	Extent <sup>b</sup> (arcsec)	Extent (kpc)	Type
1	PG 0851+203	OJ 287	08 <sup>h</sup> 54 <sup>m</sup> 48 <sup>s</sup> .87	+20°06′30″.64	0.306501	20	87	BL Lac
2	PG 1101+384	Mrk 421	11 <sup>h</sup> 04 <sup>m</sup> 27 <sup>s</sup> .31	+38°12′31″.79	0.030893	30	18	BL Lac
3	PG 1218+304	RBS 1100	12 <sup>h</sup> 21 <sup>m</sup> 21 <sup>s</sup> .94	+30°10′37″.16	0.184537	45	134	BL Lac
4	PG 1418+546	OQ +530	14 <sup>h</sup> 19 <sup>m</sup> 46 <sup>s</sup> .59	+54°23′14″.78	0.152845	45	115	BL Lac
5	PG 1424+240	OQ +240	14 <sup>h</sup> 27 <sup>m</sup> 00 <sup>s</sup> .39	+23°48′00″.03	0.160680 <sup>c</sup>	45	290	BL Lac
6	PG 1437+398	RBS 1414	14 <sup>h</sup> 39 <sup>m</sup> 17 <sup>s</sup> .47	+39°32′42″.80	0.344153	25	117	BL Lac
7	PG 1553+113	RBS 1538	15 <sup>h</sup> 55 <sup>m</sup> 43 <sup>s</sup> .04	+11°11′24″.36	0.360365	60	290	BL Lac
8	PG 2254+075	OY +091	22 <sup>h</sup> 57 <sup>m</sup> 17 <sup>s</sup> .30	+07°43′12″.30	0.188765	60	181	BL Lac
9	PG 1302−102	RBS 1212	13 <sup>h</sup> 05 <sup>m</sup> 33 <sup>s</sup> .01	−10°33′19″.43	0.27949	15	61	FSRQ
10	PG 2209+184	II Zw 171	22 <sup>h</sup> 11 <sup>m</sup> 53 <sup>s</sup> .88	+18°41′49″.85	0.06873	12	15	FSRQ
11	PG 1425+267	Ton 202	14 <sup>h</sup> 27 <sup>m</sup> 35 <sup>s</sup> .60	+26°32′14″.54	0.364262	218	1060	SSRQ
12	PG 1512+370	4C +37.43	15 <sup>h</sup> 14 <sup>m</sup> 43 <sup>s</sup> .06	+36°50′50″.35	0.370922	58	287	SSRQ
13	PG 1545+210	3C 323.1	15 <sup>h</sup> 47 <sup>m</sup> 43 <sup>s</sup> .53	+20°52′16″.61	0.264659	70	275	SSRQ
14	PG 2251+113	4C +11.72	22 <sup>h</sup> 54 <sup>m</sup> 10 <sup>s</sup> .42	+11°36′38″.74	0.32427	15	68	SSRQ
15	PG 2308+098	4C +09.72	23 <sup>h</sup> 11 <sup>m</sup> 17 <sup>s</sup> .75	+10°08′15″.75	0.432064	83	447	SSRQ

**Notes.** Column (1): serial number. Column (2): PG names of sources. Column (3): other common names of sources. Column (4): R.A. Column (5): decl. Column (6): redshift. Column (7): radio extents in arcseconds. Column (8): radio extents in kiloparsecs. Column (9): type of blazar.

<sup>a</sup> All redshift values reported are from the NASA/IPAC Extragalactic Database (NED) corrected to the reference frame defined by the 3K CMB on NED. (The NASA/IPAC Extragalactic Database (NED) is operated by the Jet Propulsion Laboratory, California Institute of Technology, under contract with the National Aeronautics and Space Administration.)

<sup>b</sup> Radio extents derived from P. Miller et al. (1993) at 5 GHz or from 1.4 GHz VLA FIRST / NVSS images for sources unresolved at 5 GHz.

<sup>c</sup>  $z = 0.60468$  has been suggested by S. Paiano et al. (2017). We have used this updated value of  $z = 0.60468$  in our calculations.

Throughout this paper we have adopted a  $\Lambda$ CDM cosmology with  $H_0 = 73 \text{ km s}^{-1} \text{ Mpc}^{-1}$ ,  $\Omega_m = 0.3$ , and  $\Omega_v = 0.7$  and used the flat  $\Lambda$ CDM subroutine of `astropy.cosmology` sub-package (Astropy Collaboration et al. 2013, 2018). The spectral index  $\alpha$  is defined such that flux density at frequency  $\nu$ ,  $S_\nu \propto \nu^\alpha$ .

## 2. The PG “Blazar” Sample

With the intention of selecting a radio unbiased blazar sample, we chose the Palomar-Green UV-excess survey (R. F. Green et al. 1986) as the parent sample. It remains the largest complete optically selected survey for unobscured AGN at low redshift and is one of the most well-studied samples of AGN having extensive supplementary multiband data available in the literature (K. I. Kellermann et al. 1989; T. A. Boroson & R. F. Green 1992; P. Miller et al. 1993).

The sample selection is described in J. Baghel et al. (2023). The key points for the sample presented here are as follows:

1. We selected the 16 RL quasars and 8 BL Lac objects to form the PG “blazar” sample based on (i) a redshift cut-off ( $z < 0.5$ ), as well as (ii) having core-to-lobe extents greater than  $\geq 15''$ . This was to ensure that these blazars could be well resolved with both the VLA 1'' and the uGMRT 5'' resolution observations.
2. The sample includes steep-spectrum radio quasars (SSRQs) along with the flat-spectrum radio quasars (FSRQs) to create a statistically representative sample. The kiloparsec-scale polarization properties would be negligibly affected by jet orientation between these two quasar subclasses.
3. This paper completes the VLA observations of the PG sample with the remaining seven quasars and eight BL Lac objects with new observations (See Tables 1–4 and 5 and 6).

## 3. Radio Data Analysis

The radio data for these blazars were obtained with the VLA in C-band (6 GHz) in B-array to BnA  $\rightarrow$  A array configurations from 2023 January 15 to 2023 June 22 (Project ID: 23A-038) with a resolution of 1''1 as noted in Table 6. The frequency range of 4.5–6.6 GHz was spanned by 16 spectral windows with 64 channels each. The average time on source was around 40 minutes. Polarization calibrators 3C 286 and 3C 138 were used. For the initial calibration and flagging, we employed the CASA calibration pipeline for VLA data reduction. We followed this with manual polarization calibration.

Initially, the CASA task `SETJY` was used to manually configure the model of a polarized calibrator. As the model parameters, we used the reference frequency, Stokes  $I$  flux density at the reference frequency, and the spectral index. The inputs also included the coefficients of the Taylor expansion of fractional polarization and polarization angle as a function of frequency, centered on the reference frequency, which was estimated by fitting a first-order polynomial to the values obtained from the NRAO VLA observing guide.<sup>9</sup> The R. A. Perley & B. J. Butler (2017) scale was used to estimate the Stokes  $I$  flux density values, the spectral index ( $\alpha$ ), and also the curvature ( $\beta$ ) about the reference frequency.

The process of polarization calibration involves three stages. (i) The task `GAINCAL` with `gaintype = KCROSS` in CASA was used to solve for the cross-hand (RL, LR) delays, using a polarized calibrator (either 3C 138 or 3C 286). (ii) The task `POLCAL` in CASA was used to solve for instrumental polarization (i.e., the leakage terms or “D-terms”). The task `POLCAL` with `poltype = Df + QU` was used when using the polarized calibrators (either 3C 138 or 3C 286), and `poltype = Df` was used when using the unpolarized calibrator

<sup>9</sup> <https://science.nrao.edu/facilities/vla/docs/manuals/obsguide/modes/pol>



**Table 2**  
Observational Parameters from the VLA Images of PG BL Lacs and Seven PG Quasars

Source	$I_{\text{rms}}$ ( $\mu\text{Jy beam}^{-1}$ )	$P_{\text{rms}}$ ( $\mu\text{Jy beam}^{-1}$ )	Region		$P$ (mJy)	$I$ (mJy)	FP (%)	$\alpha$
BL Lacs								
PG 0851+203	920	585	Core		$209 \pm 19$	3841.4	$13 \pm 2$	$0.50 \pm 0.09$
PG 1101+385	56.2	188	Core		$17 \pm 1$	394	$16 \pm 2$	$-0.22 \pm 0.06$
PG 1218+304	12.6	8.7	Core		$1.8 \pm 0.1$	487	$17 \pm 1$	$-0.12 \pm 0.01$
PG 1418+546	157	296	Core		$35 \pm 2$	638	$3.59 \pm 0.05$	$-0.14 \pm 0.03$
PG 1424+240	99	110	Core		$16.5 \pm 0.7$	360	$18.6 \pm 0.9$	$-0.16 \pm 0.04$
			Lobes	N	$16 \pm 3$	30	$24 \pm 6$	... <sup>a</sup>
				S	$17 \pm 2$	21	$33 \pm 6$	... <sup>a</sup>
PG 1437+398	24.8	16.6	Core		$2.39 \pm 0.07$	48.3	$17 \pm 2$	$-0.23 \pm 0.04$
			Lobes	S	$5.3 \pm 0.5$	3.15	... <sup>a</sup>	... <sup>a</sup>
PG 1553+113	157	15.8	Core		$17.6 \pm 0.3$	321	$14 \pm 2$	$-0.07 \pm 0.02$
PG 2254+075	174	131	Core		$14 \pm 4$	601	$1.1 \pm 0.7$	$0.20 \pm 0.09$
Quasars: FSRQs								
PG 1302−102	116	42.9	Core		$21.2 \pm 0.6$	682	$9.8 \pm 0.7$	$-0.3 \pm 0.1$
			Lobes	NE (up)	$6.9 \pm 0.6$	21.8	... <sup>a</sup>	... <sup>a</sup>
				SE (up)	$3.8 \pm 0.2$	3.46	... <sup>a</sup>	... <sup>a</sup>
PG 2209+184	85.8	32.3	Core		$1.0 \pm 0.1$	108	$1.50 \pm 1.1$	$-0.7 \pm 0.1$
Quasars: SSRQs								
PG 1425+267	7.45	2.77	Core		$0.87 \pm 0.06$	26	$9.5 \pm 0.9$	$-0.4 \pm 0.1$
			Lobes	NE (up)	$0.09 \pm 0.03$	5.68	... <sup>a</sup>	... <sup>a</sup>
				SW (dn)	$4.4 \pm 0.7$	30.2	$30 \pm 5$	$-1.2 \pm 0.1$
			Jet	SW	$0.5 \pm 0.1$	1.58	... <sup>a</sup>	... <sup>a</sup>
PG 1512+370	8.88	3.77	Core		$0.96 \pm 0.07$	43.1	$10 \pm 2$	$-0.33 \pm 0.01$
			Hot spot	W	$7.7 \pm 0.2$	37.4	$21 \pm 2$	$-0.65 \pm 0.04$
				E	$8.55 \pm 0.09$	50.5	$16.3 \pm 0.4$	$-0.91 \pm 0.03$
			Lobes	W	$18 \pm 2$	86.4	$25 \pm 4$	$-1.09 \pm 0.09$
				E	$20 \pm 1$	105	$22 \pm 3$	$-0.88 \pm 0.08$
PG 1545+210	20.2	13.3	Core		$1.4 \pm 0.2$	46.4	$5.1 \pm 0.5$	$-0.1 \pm 0.1$
			Hot spot	N	$33.7 \pm 0.5$	354	$20.8 \pm 0.9$	$-0.9 \pm 0.03$
				S	$16.5 \pm 0.3$	162	$16 \pm 1$	$-0.91 \pm 0.01$
			Lobes	N	$23 \pm 3$	60.3	$37 \pm 6$	... <sup>a</sup>
				S	$11.8 \pm 0.3$	65.1	$26 \pm 5$	... <sup>a</sup>
			Jet	S	$1.5 \pm 2$	10.5	$20 \pm 4$	... <sup>a</sup>
PG 2251+113	29	7.9	Core		$0.6 \pm 0.1$	31.5	$3.6 \pm 0.7$	$-0.13 \pm 0.01$
			Lobes	NW	$6.2 \pm 0.6$	165	$7 \pm 1$	$-0.70 \pm 0.06$
				SE	$15.5 \pm 0.8$	315	$7.3 \pm 0.9$	$-0.9 \pm 0.1$
PG 2308+098	49	10.6	Core		$2.6 \pm 0.1$	88.7	$4.2 \pm 0.6$	$0.08 \pm 0.01$
			Lobes	SE	$4 \pm 1$	37.8	$30 \pm 8$	$-1.1 \pm 0.3$
			Hot spot	SE	$3.3 \pm 0.3$	45.6	$10 \pm 1$	$-1.0 \pm 0.2$
				NW T1	$0.38 \pm 0.06$	7.24	$9 \pm 2$	$-1.2 \pm 0.1$
			Jet knots	NW T2	$1.7 \pm 0.1$	20.7	$10 \pm 2$	$-0.86 \pm 0.05$
				NW T3	$0.20 \pm 0.06$	7.25	$11 \pm 4$	$-1.2 \pm 0.2$
				NW T4	$0.07 \pm 0.02$	0.648	$19 \pm 5$	$-1.5 \pm 0.3$

**Notes.** Column (1): PG source name. Column (2): rms noise in Stokes  $I$  (total intensity) image. Column (3): rms noise in the polarized intensity image. Column (4): region of the source. Column (5): polarized flux density. Column (6): total flux density. Column (7): fractional Polarization. Column (8): spectral index.

<sup>a</sup> High error values.

(3C 84). The average value of the D-term amplitude turned out to be  $\approx 7\%$ . (iii) The task POLCAL in CASA with poltype = Xf was used to solve for the frequency-dependent polarization angle using a polarized calibrator (either 3C 138 or 3C 286) with a known EVPA. These calibration solutions were subsequently applied to the data set.

The calibrated visibility data for the sources were extracted using the CASA task SPLIT, which also averaged the spectral channels such that bandwidth (BW) smearing effects were negligible. The multiterm-multifrequency synthesis (MT-MFS;

U. Rau & T. J. Cornwell 2011) algorithm of the TCLEAN task in CASA was used to then create the total intensity or the Stokes  $I$  image of the sources. Three rounds of phase-only self-calibration followed by one round of amplitude and phase self-calibration were carried out for almost all the data sets, except those for PG 1545+210 and PG 2308+098, for which only two rounds of phase-only self-calibration were carried out. Images were created using natural weighting with robust=+0.5 in CASA. The final self-calibrated visibility data were used to create the Stokes  $Q$  and  $U$  images.

**Table 3**  
The PG “Blazar” Sample Properties

S.No.	Name	Type	$\log_{10} \frac{M_{\text{BH}}}{M_{\odot}}$	References	$\bar{Q}$ ( $10^{42} \text{ erg s}^{-1}$ )	$L_{\gamma}$ ( $\text{erg s}^{-1}$ )	$\log_{10}(\nu_s/\text{Hz})$	$\log_{10} \dot{M}$ ( $\frac{M_{\odot}}{\text{yr}}$ )	References
1	PG 0851+203	BL Lac	8.5	(1)	210	$(1.62 \pm 0.04) \times 10^{46}$	13.24	...	...
2	PG 1101+384	BL Lac	8.23	(1)	6.58	$(8.4 \pm 0.1) \times 10^{44}$	16.22	...	...
3	PG 1218+304	BL Lac	8.47	(1)	9.23	$(4.0 \pm 0.1) \times 10^{45}$	16.27	...	...
4	PG 1418+546	BL Lac	8.74	(1)	61.80	$(7.3 \pm 0.4) \times 10^{44}$	13.68	...	...
5	PG 1424+240	BL Lac	6.42	(1)	988	$(1.47 \pm 0.03) \times 10^{47}$	15.29	...	...
6	PG 1437+398	BL Lac	8.95	(1)	165	$(2.2 \pm 0.2) \times 10^{45}$	15.86	...	...
7	PG 1553+113	BL Lac	7.25	(1)	120	$(6.6 \pm 0.1) \times 10^{46}$	15.59	...	...
8	PG 2254+075	BL Lac	8.85	(1)	43	$(3.4 \pm 0.5) \times 10^{44}$	12.78	...	...
9	PG 0007+106	FSRQ	8.87	(2)	7.01	...	...	-0.42	(3)
10	PG 1226+023	FSRQ	9.18	(2)	4850	...	...	1.18	(3)
11	PG 1302-102	FSRQ	9.05	(2)	161	...	...	0.92	(3)
12	PG 1309+355	FSRQ	8.48	(2)	9.92	...	...	0.37	(3)
13	PG 2209+184	FSRQ	8.89	(2)	1.50	...	...	-0.98	(3)
14	PG 0003+158	SSRQ	9.45	(2)	2380	...	...	0.79	(3)
15	PG 1004+130	SSRQ	9.43	(2)	847	...	...	-0.37	(4)
16	PG 1048-090	SSRQ	9.37	(2)	2690	...	...	0.3	(3)
17	PG 1100+772	SSRQ	9.44	(2)	3540	...	...	0.29	(3)
18	PG 1103-006	SSRQ	9.49	(2)	2250	...	...	0.21	(3)
19	PG 1425+267	SSRQ	9.9	(2)	519	...	...	0.07	(3)
20	PG 1512+370	SSRQ	9.53	(2)	1920	...	...	0.2	(3)
21	PG 1545+210	SSRQ	9.47	(2)	1930	...	...	0.01	(3)
22	PG 1704+608	SSRQ	9.55	(2)	4640	...	...	0.38	(3)
23	PG 2251+113	SSRQ	9.15	(2)	1760	...	...	0.66	(3)
24	PG 2308+098	SSRQ	9.76	(2)	2000	...	...	0.22	(3)

**Notes.** Column (1): serial number. Column (2): PG names. Column (3): blazar type. Column (4): black hole masses. Column (5): references for black hole masses. Column (6): jet power. Column (7): gamma-ray luminosity (0.1–100 GeV) from S. Abdollahi et al. (2022). Column (8): synchrotron peak frequency from S. Abdollahi et al. (2022). Column (9): accretion rates. Column (10): references for accretion rates.

**References.** (1): Z.-Z. Wu et al. (2009), (2): J. Shanguan et al. (2018), (3): S. W. Davis & A. Laor (2011), (4): B. Luo et al. (2013).

**Table 4**  
Observational Results from J. Baghel et al. (2023)

Source	Region	$P$ (Jy)	$I$ (Jy)	FP (%)	$\alpha$
PG 0003+158	Core	$(3.6 \pm 0.8) \text{ E-04}$	1.65E-01	$8\% \pm 2\%^a$	$-0.13 \pm 0.13$
PG 0007+106	Core	$(1.2 \pm 0.3) \text{ E-04}$	1.26E-01	$0.8\% \pm 0.3\%$	$0.12 \pm 0.03$
PG 1004+130	Core	$(2.7 \pm 0.8) \text{ E-05}$	2.90E-02	$3\% \pm 1\%^b$	$-0.3 \pm 0.2$
PG 1048-090	Core	$(8 \pm 2) \text{ E-05}$	4.9798E-02	$2.1\% \pm 0.4\%$	$0.2 \pm 0.4$
PG 1100+772	Core	$(1.17 \pm 0.05) \text{ E-03}$	1.17E-01	$2.7\% \pm 0.4\%$	$0.55 \pm 0.006$
PG 1103-006	Core	$(2.08 \pm 0.07) \text{ E-03}$	1.37E-01	$5.8\% \pm 0.3\%$	$-0.319 \pm 0.004$
PG 1226+023	Core	$(2.128 \pm 0.009) \text{ E+00}$	2.16E+01	$11\% \pm 2\%$	$-0.327 \pm 0.004$
PG 1309+355	Core	$(1.3 \pm 0.2) \text{ E-04}$	4.69E-02	$0.37\% \pm 0.07\%$	$0.17 \pm 0.06$
PG 1704+608	Core	$(1.36 \pm 0.08) \text{ E-03}$	2.12E-02	$8.2\% \pm 0.9\%$	$-0.8 \pm 0.7$

**Notes.** Column (1): PG source name. Column (2): region of the source and location. Column (3): polarized flux density. Column (4): total flux density. Column (5): fractional polarization. Column (6): spectral index.

<sup>a</sup> FP at intensity peak position is  $0.9\% \pm 0.3\%$ .

<sup>b</sup> FP at intensity peak position is  $0.27\% \pm 0.09\%$ .

The Stokes  $Q$  and  $U$  images were combined to produce the linear polarized intensity  $P = \sqrt{Q^2 + U^2}$  and EVPA or  $\chi = 0.5 \tan^{-1}(U/Q)$  images using the AIPS<sup>10</sup> task COMB with opcode = POLC (which corrects for Ricean bias) and POLA, respectively. COMB blanked regions with polarized intensity values  $< 3 \times$  the rms noise in the  $P$  image and regions with values greater than  $10^\circ$  error in the  $\chi$  image. The COMB task with opcode = DIV was then used to get the fractional

polarization  $\text{FP} = P/I$  images with regions with  $\gtrsim 10\%$  fractional polarization errors blanked.

The in-band spectral index images and spectral index noise images are produced while imaging with the MT-MFS algorithm of the TCLEAN task in CASA with two Taylor terms to model the frequency dependence of the sky emission by setting the parameter nterms = 2. We used AIPS to blank the regions with spectral index noise greater than about 0.3. This varied by image and was chosen such that regions with total intensity  $> 3 \times$  rms noise are included. In cases of high

<sup>10</sup> Astronomical Image Processing System; D. C. Wells (1985).

noise, we also blanked the spectral index noise image using the same.

The average rms noise in the Stokes  $I$  images is  $1.28 \times 10^{-4}$  mJy beam $^{-1}$ . The values obtained from the images are presented in Table 2. Flux density values reported in the paper were obtained using the Gaussian-fitting AIPS task JMFIT for compact components like the core, and the AIPS verb TVSTAT for extended emission. Care was taken to exclude the compact regions from selection for obtaining values only for the extended regions using TVSTAT. The FP and spectral index values noted are the mean values over the noted region. The errors in these values are noted from the mean values over the same region for the corresponding noise image. We note here that since these values are the average over a region, they may include blanked regions in the noise image especially in regions of diffuse and patchy emission leading to higher reported noise values in such regions. In Table 2 we have not reported values for regions where noise was exceptionally high. The rms noise values were obtained using AIPS tasks TVWIN and IMSTAT. The AIPS procedure TVDIST was used to obtain spatial extents.

We note that Faraday rotation effects are not expected to be significant at 5 GHz in the kiloparsec-scale observations of jets and lobes (e.g., D. J. Saikia et al. 1987; R. E. Pudritz et al. 2012). Integrated RM  $\lesssim 50$  rad m $^{-2}$  results in rotation of  $\lesssim 10^\circ$  at 5 GHz. RM values can indeed be higher than the integrated RM values in smaller local regions, which can influence the local inferred B-field directions (e.g., J. P. McKean et al. 2016; S. Silpa et al. 2021b). However, the absence of strong Faraday effects is supported by the observed polarization in the jets in these sources, which tend to lie either parallel or perpendicular to the local jet direction, with the inferred B-field directions being perpendicular to the direction of the EVPA vectors for optically thin regions of emission; such orientations could be indicative of organized B-field structures (see R. E. Pudritz et al. 2012).

#### 4. Results from New Data

The VLA 6 GHz polarization images and in-band spectral index images of the eight BL Lac objects and the seven RL quasars are presented here in Figures 1–15. The results have also been listed in Table 2. The fractional polarization ranges from  $1.1\% \pm 0.7\%$  to  $37\% \pm 6\%$  in the radio cores, lobes, and hot spots of these blazars. The radio cores are mostly flat or inverted in the spectral index images with a few slightly steeper values occurring where it is hard to discern the boundary of the core with portions of the inner jet. The hot spots in several of the quasars are steeper than typical values of about  $-0.5$  to  $-0.7$  (J. J. Harwood et al. 2013), ranging from  $-0.7 \pm 0.1$  up to  $-1.0 \pm 0.20$ , as also seen in J. Baghel et al. (2023), indicating bow-shock-like structures that could arise due to episodic AGN activity (D. A. Clarke et al. 1992; S. Silpa et al. 2021a; S. Ghosh et al. 2023). Below we discuss the PG BL Lac objects collectively (see individual notes in J. Baghel et al. 2024) and the PG quasars individually.

##### 4.1. PG BL Lac Objects

In this section, we describe the VLA results for the PG BL Lacs. The uGMRT data on these BL Lacs have been presented in J. Baghel et al. (2024). We find that six out of eight PG BL Lacs show compact core-halo structures with the exception of

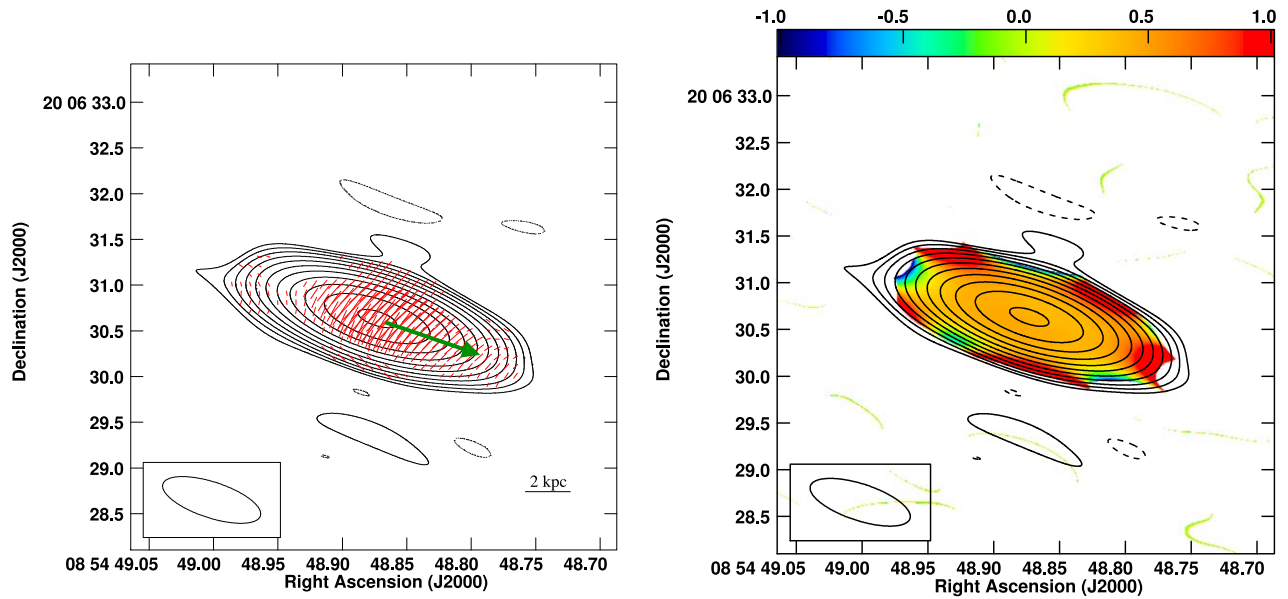
PG 1424+240, which shows diffuse lobes to the north and south, and PG 1437+398, whose diffuse lobe extends to the southwest.

Table 5 lists the VLBI jet directions in the PG blazars with the parsec-scale mean jet PA obtained from multifrequency (1.4–86 GHz), multiepoch VLBA observations of A. V. Plavin et al. (2022) and 5 GHz VLBI imaging of A. Wang et al. (2023). Our VLA 6 GHz image shows core EVPA perpendicular to the source’s VLBI jet direction for PG 0851+203 (Figure 1) and PG 1418+546 (Figure 4). PG 1437+398 (Figure 6) also displays core EVPA perpendicular to this source’s indicated diffuse lobe and possible jet direction. The diffuse lobe is also polarized, although the errors in fractional polarization are high with no uniformity in the EVPA patterns in the lobe. The EVPA structures in the uGMRT 650 MHz images of J. Baghel et al. (2024) of PG 0851+203, PG 1418+546, and PG 1437+398 are consistent with that of the new VLA images and are perpendicular to the jet direction in the case of PG 0851+203 and PG 1437+398, but are parallel in the case of PG 1418+546. PG 1418+546 also shows a hot spot to the east in its uGMRT image, suggesting multiple jet reorientations in this source.

The VLA 6 GHz core EVPA for PG 1101+385 (Figure 2), PG 1218+304 (Figure 3), PG 1553+113 (Figure 7), and PG 2254+075 (Figure 8) are complex in structure. A similar complex core is observed in the uGMRT observations of PG 1101+385 and PG 2254+075, whereas PG 1218+304’s uGMRT core EVPA was perpendicular to its VLBI jet direction and in PG 1553+113 its uGMRT core EVPA was oblique to its VLBI jet direction. In PG 1553+113 our VLA core shows two components, which both have EVPA oblique to the VLBI jet direction, which lies parallel along the direction of the EVPA of the second component. Our EVPA of our uGMRT image (J. Baghel et al. 2024) matches one of these components. This could again suggest a structured jet. For PG 2254+075, the VLBI jet direction lies to the southwest and the VLA image shows some indication of EVPA parallel to the jet direction there.

Finally, PG 1424+240 (Figure 5) shows its VLA 6 GHz core EVPA parallel to its VLBI jet direction, whereas its uGMRT core EVPA was perpendicular. The double lobes seen in J. Baghel et al. (2024) are also resolved and show polarization with EVPA parallel along the outflowing lobes. This is in contrast to the uGMRT image where the lobes had EVPA perpendicular along the outflowing lobes, possibly suggesting a spine-sheath structured jet. However, we note that the diffuse lobe emission was patchy in both total intensity and polarized intensity, and as such the values of fractional polarization and spectral index are not reliable for these regions.

Overall, three out of eight of the BL Lacs have their EVPA perpendicular to the jet direction, one shows a spine-sheath-like structure, and the remaining four show complex EVPA structures suggesting jet reorientations or turbulent magnetic fields. Of the three that have EVPA perpendicular to the jet direction, two are LSP BL Lacs with indications of terminal hot spots in their uGMRT images similar to FR type II radio galaxies. A. V. Plavin et al. (2022) have provided a mean jet PA of these BL Lacs with multifrequency, multiepoch gigahertz VLBA observations that have been denoted in the figures and mentioned in Table 5. These differ from the multiepoch 15 GHz VLBA mean jet PA provided by M. L. Lister et al. (2021) and noted in our J. Baghel et al. (2024) paper by an average of  $\sim 5^\circ$ ,



**Figure 1.** VLA 6 GHz contour image of BL Lac PG 0851+203 superimposed with (left) red polarized intensity vectors and (right) the in-band spectral index image. The VLBI jet direction is shown by the green arrow. The beam is  $1''.12 \times 0''.39$  with a PA of  $72^\circ$ . The peak surface brightness,  $I_p$ , is  $3.833 \text{ Jy beam}^{-1}$  and the contour levels are  $I_p \times 10^{-2} \times (-0.09, 0.09, 0.18, 0.35, 0.7, 1.4, 2.8, 5.6, 11.25, 22.5, 45, 90) \text{ Jy beam}^{-1}$ . A  $1''$  length of the vector corresponds to  $0.25 \text{ Jy beam}^{-1}$ .

except for PG 1553+113 and PG 2254+075 where it differs by  $34^\circ$  and  $13^\circ$ , respectively.

#### 4.2. PG Quasars

VLA images of nine of the sixteen PG quasars have been previously presented in J. Baghel et al. (2023). Here, we discuss the VLA 6 GHz images of the remaining seven quasars. Additional notes on individual sources are provided in the Appendix.

Of the seven quasars presented in this paper, the FSRQ PG 2209+184 displays a compact structure, whereas the other FSRQ PG 1302-102 and all SSRQs (Figures 9, 11–15) display extended polarized emission. PG 1302-102 displays a bow-shaped diffuse emission around its core toward the east but without a well-defined hot spot. SSRQs PG 1512+370, PG 1545+210, and PG 2251+113 display typical FR II-like double radio structures with well-defined lobes and hot spots (except for PG 2251+113 for which higher-resolution imaging than the one presented is needed to see hot spots). PG 2308+098 shows multiple jet knots in its northern jet and no clear hot spot or diffuse lobe to the north. PG 1425+267 displays a large ( $\sim 1 \text{ Mpc}$ ) source with the southwestern approaching jet's hot spot discernible in both total intensity and polarization, while no hot spot is visible in the counterjet lobe.

##### 4.2.1. PG 1302-102

This FSRQ (Figure 9) at a redshift of  $z = 0.279$  was first imaged at 1.4 GHz and 6 GHz by A. C. Gower & J. B. Hutchings (1984), who found a  $15''$  two-sided radio structure with radio lobes to the northeast and the southeast and a 570 mJy core at 1.4 GHz. The projected bending angle between the two lobes is  $60^\circ$  (T. A. Rector et al. 1995). The bent shape of the extended radio emission is over 45 kpc and suggests that the radio source is relatively old and/or not well confined. A 1.4 GHz VLBI image by J. B. Hutchings & S. G. Neff (1992) and a 5 GHz VLBI image by A. Wang et al.

(2023) show an unresolved core. Some 15 GHz VLBA observations have provided a mean jet PA of  $32^\circ$  (M. L. Lister et al. 2021), which agrees with the average jet PA of A. V. Plavin et al. (2022). Our VLA 6 GHz observations for this FSRQ match those of A. C. Gower & J. B. Hutchings (1984) with the diffuse emission being patchy and with the northeastern lobe picked up better than the southeastern one. The core EVPA is perpendicular to the VLBI jet and the northeastern lobe; however, no distinct hot spots can be detected. The values of fractional polarization and spectral index are not reliable for the patchy lobe emission.

##### 4.2.2. PG 2209+184

For this FSRQ (Figure 10), the total 5 GHz VLA flux density has been previously measured to lie between 120 mJy (P. Miller et al. 1993) and 290 mJy (K. I. Kellermann et al. 1989; claimed by Miller et al. to be an error). It has been found to have a variable flux density at 5 GHz of between 116 mJy and 326 mJy (J. Machalski & P. Magdziarz 1993) and is classified as a radio intermediate quasar (H. Falcke et al. 1995). The core is the prominent feature, with the core flux density accounting for  $>95\%$  of the total flux. There is a low-brightness knot toward the northeast. It has an inverted spectrum between 5 GHz and 1.4 GHz with an  $\alpha = -0.24$  (H. Falcke et al. 1995). The parsec-scale 5 GHz VLBI image by A. Wang et al. (2023) shows a jet to the northeast. A. V. Plavin et al. (2022) indicate an average jet PA of  $21^\circ$ . This FSRQ shows a compact core with some diffuse core-halo emission to the northeast in our VLA 6 GHz observations. The core EVPA is complex. However, the EVPA toward the northeast of the core in the direction of the VLBI jet shows EVPA parallel to the jet direction.

##### 4.2.3. PG 1425+267

This SSRQ (Figure 11) has a very large radio extent of about 1.5 Mpc (K. I. Kellermann et al. 1994). It has a clear double-



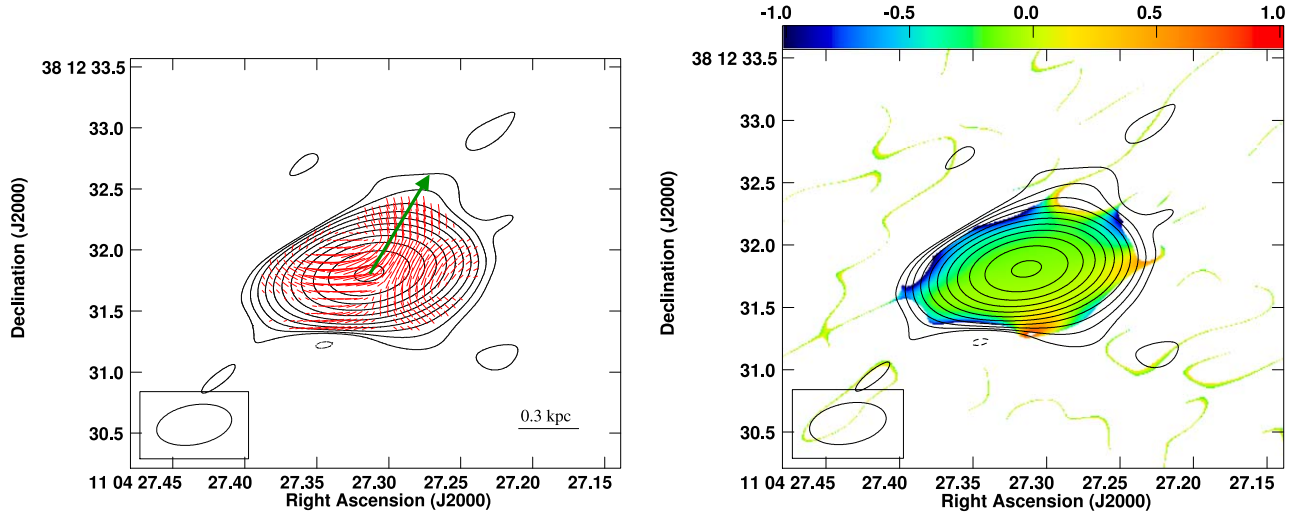


**Figure 2.** VLA 6 GHz contour image of BL Lac PG 1101+384 superimposed with (left) red polarized intensity vectors and (right) the in-band spectral index image. The VLBI jet direction is shown by the green arrow. The beam is  $0''.62 \times 0''.32$  with a PA of  $-80^\circ$ . The peak surface brightness,  $I_p$ , is  $0.38 \text{ Jy beam}^{-1}$  and the contour levels are  $I_p \times 10^{-2} \times (-0.09, 0.09, 0.18, 0.35, 0.7, 1.4, 2.8, 5.6, 11.25, 22.5, 45, 90) \text{ Jy beam}^{-1}$ . A  $1''$  length of the vector corresponds to  $25 \text{ mJy beam}^{-1}$ .

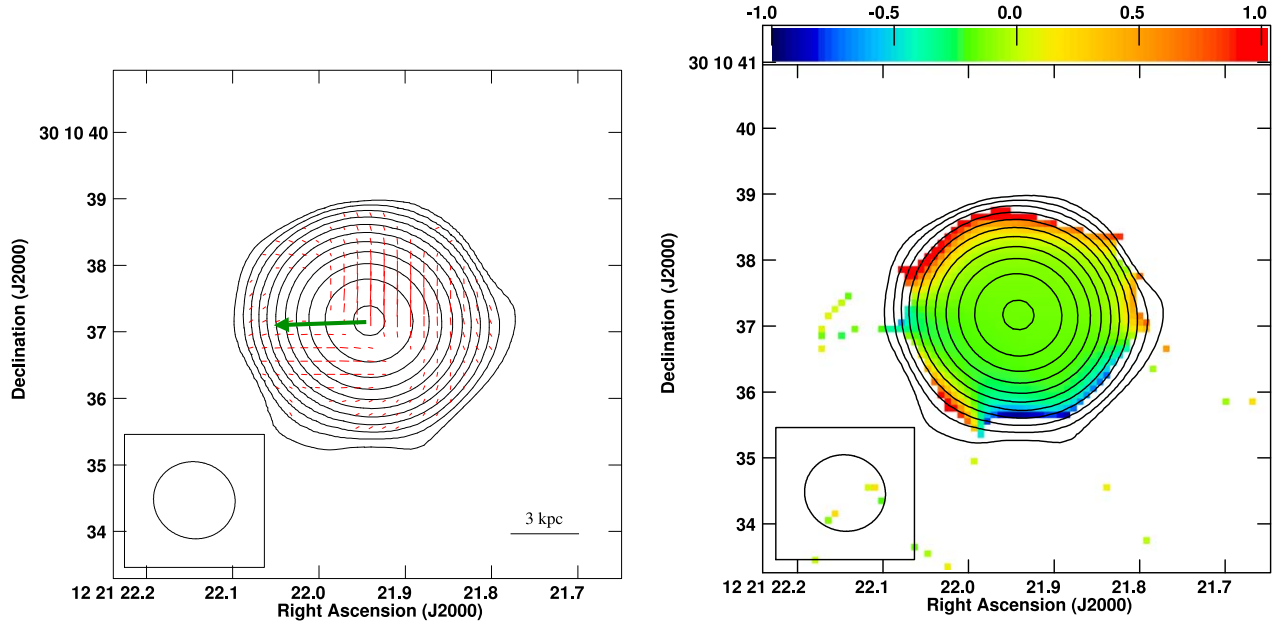


**Figure 3.** VLA 6 GHz contour image of BL Lac PG 1218+304 superimposed with (left) red polarized intensity vectors and (right) the in-band spectral index image. The VLBI jet direction is shown by the green arrow. The beam is  $1''.23 \times 1''.15$  with a PA of  $76^\circ$ . The peak surface brightness,  $I_p$ , is  $48.3 \text{ mJy beam}^{-1}$  and the contour levels are  $I_p \times 10^{-2} \times (-0.09, 0.09, 0.18, 0.35, 0.7, 1.4, 2.8, 5.6, 11.25, 22.5, 45, 90) \text{ Jy beam}^{-1}$ . A  $1''$  length of the vector corresponds to  $2.5 \text{ mJy beam}^{-1}$ .

lobed structure with a faint jet observed extending toward the southwestern component from the core. The parsec-scale 5 GHz VLBI image by A. Wang et al. (2023) shows a jet to the southwest. We find our VLA 6 GHz observations of this SSRQ match those of K. I. Kellermann et al. (1994), and the southwestern jet shows polarized emission in its hot spot with EVPA typical of B-field compression. The jet and the northeastern lobe emission are very diffuse and barely polarized, with high errors in their fractional polarization. The core EVPA is perpendicular to the jet direction.

#### 4.2.4. PG 1512+370

This SSRQ (Figure 12) has the radio morphology of a typical linear and symmetrical FR II radio galaxy, with the distance between the hot spots being  $60''$  (370 kpc) at a position angle of

$110^\circ$  (P. Miller et al. 1993). The parsec-scale 5 GHz VLBI image by A. Wang et al. (2023) shows a tentative jet to the northwest. The VLA 6 GHz observations for this SSRQ (Figure 12) are consistent with those of P. Miller et al. (1993), showing hot spots with EVPA characteristic of B-field compression, and more of the diffuse lobe emission is detected. The EVPA of the core is orthogonal to the jet direction.

#### 4.2.5. PG 1545+210

This SSRQ (Figure 13) at a redshift of  $z = 0.264$  is one of the nearest 3C quasars. The triple radio structure was identified in early 5 GHz maps by G. G. Pooley & S. N. Henbest (1974). Even though earlier radio images of this source existed (W. J. Bogers et al. 1994), the VLA 1.4 GHz A-array image was the first to identify the jet leading into the southern lobe. The

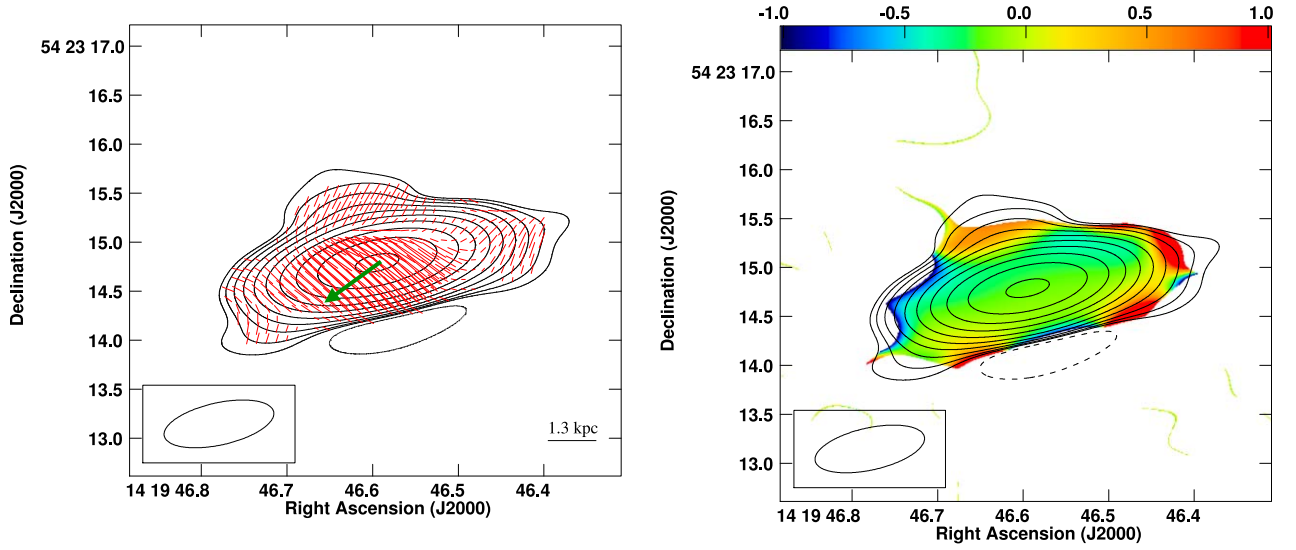


**Figure 4.** VLA 6 GHz contour image of BL Lac PG 1418+546 superimposed with (left) red polarized intensity vectors and (right) the in-band spectral index image. The VLBI jet direction is shown by the green arrow. The beam is  $1''.14 \times 0''.43$  with a PA of  $-78^\circ$ . The peak surface brightness,  $I_p$ , is  $0.63 \text{ Jy beam}^{-1}$  and the contour levels are  $I_p \times 10^{-2} \times (-0.18, 0.18, 0.35, 0.7, 1.4, 2.8, 5.6, 11.25, 22.5, 45, 90) \text{ Jy beam}^{-1}$ . A  $1''$  length of the vector corresponds to  $25 \text{ mJy beam}^{-1}$ .

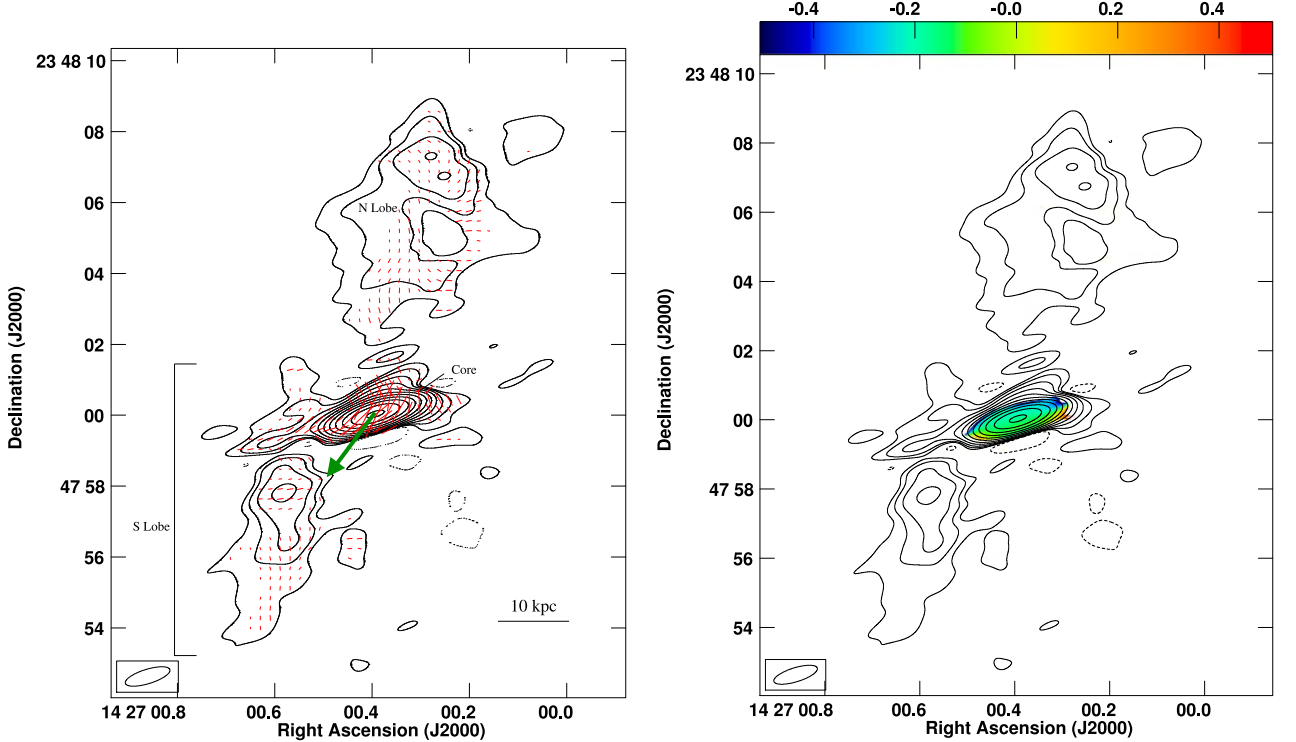


**Figure 5.** VLA 6 GHz contour image of BL Lac PG 1424+240 superimposed with (left) red polarized intensity vectors and (right) the in-band spectral index image. The VLBI jet direction is shown by the green arrow. The beam is  $1''.32 \times 0''.40$  with a PA of  $-73^\circ$ . The peak surface brightness,  $I_p$ , is  $0.35 \text{ Jy beam}^{-1}$  and the contour levels are  $I_p \times 10^{-2} \times (-0.09, 0.09, 0.18, 0.35, 0.7, 1.4, 2.8, 5.6, 11.25, 22.5, 45, 90) \text{ Jy beam}^{-1}$ . A  $1''$  length of the vector corresponds to  $5 \text{ mJy beam}^{-1}$ .

symmetric source is  $\sim 360 \text{ kpc}$  in extent, straight along its axis. The 5 GHz VLBI image by A. Wang et al. (2023) shows an unresolved core. Some 2 and 8 GHz VLBA observations have provided a mean jet PA of  $-172^\circ$  (A. V. Plavin et al. 2022). We find our VLA 6 GHz observations of this SSRQ match those of P. Miller et al. (1993) with the detection of more diffuse lobe emission and typical FR II-like polarization structures and hot spots with EVPA typical of B-field compression. The core EVPA is perpendicular to the jet direction.

#### 4.2.6. PG 2251+113

This SSRQ (Figure 14) is a relatively compact ( $\sim 75 \text{ kpc}$ ), linear radio source (J. D. H. Pilkington & J. F. Scott 1965; P. Miller et al. 1993; K. I. Kellermann et al. 1994). The parsec-scale 5 GHz VLBI image by A. Wang et al. (2023) shows an unresolved core. Some 8 GHz VLBA observations have provided a mean jet PA of  $139^\circ$  (A. V. Plavin et al. 2022). Our VLA 6 GHz observations of this SSRQ match those of P. Miller et al. (1993) with more diffuse lobe emission being

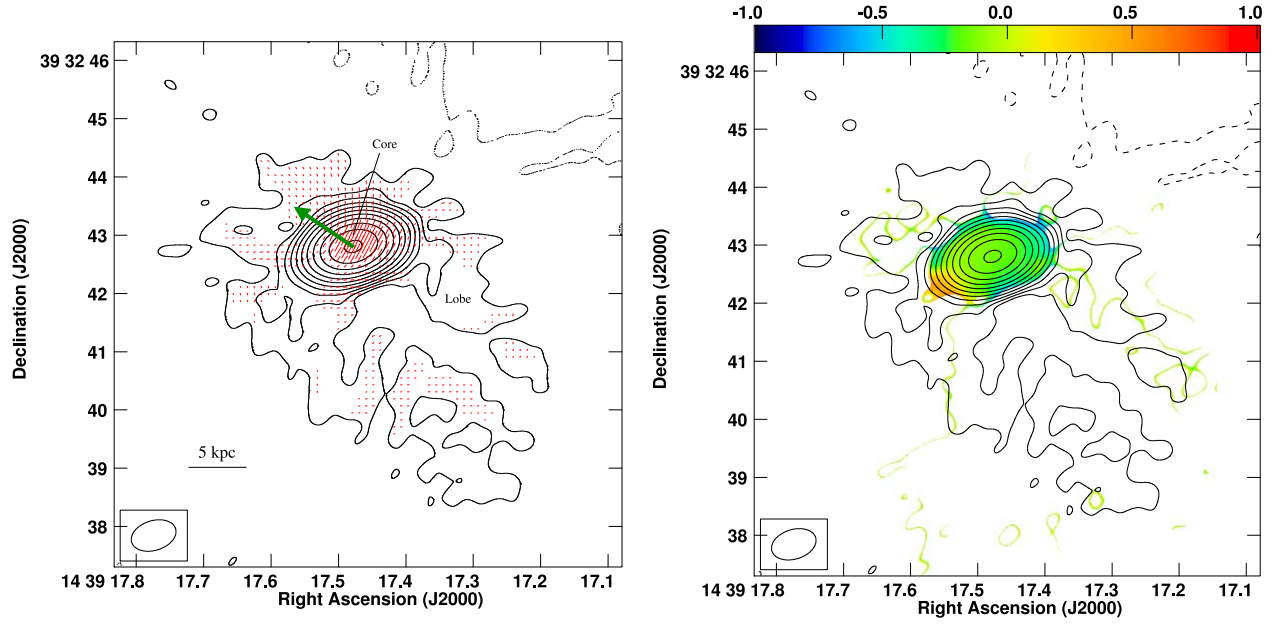


**Figure 6.** VLA 6 GHz contour image of BL Lac PG 1437+398 superimposed with (left) red polarized intensity vectors and (right) the in-band spectral index image. The beam is  $0''.79 \times 0''.51$  with a PA of  $-73^\circ$ . The peak surface brightness,  $I_p$ , is  $47.5 \text{ mJy beam}^{-1}$  and the contour levels are  $I_p \times 10^{-2} \times (-0.09, 0.09, 0.18, 0.35, 0.7, 1.4, 2.8, 5.6, 11.25, 22.5, 45, 90) \text{ Jy beam}^{-1}$ . A  $1''$  length of the vector corresponds to  $50 \text{ mJy beam}^{-1}$ .

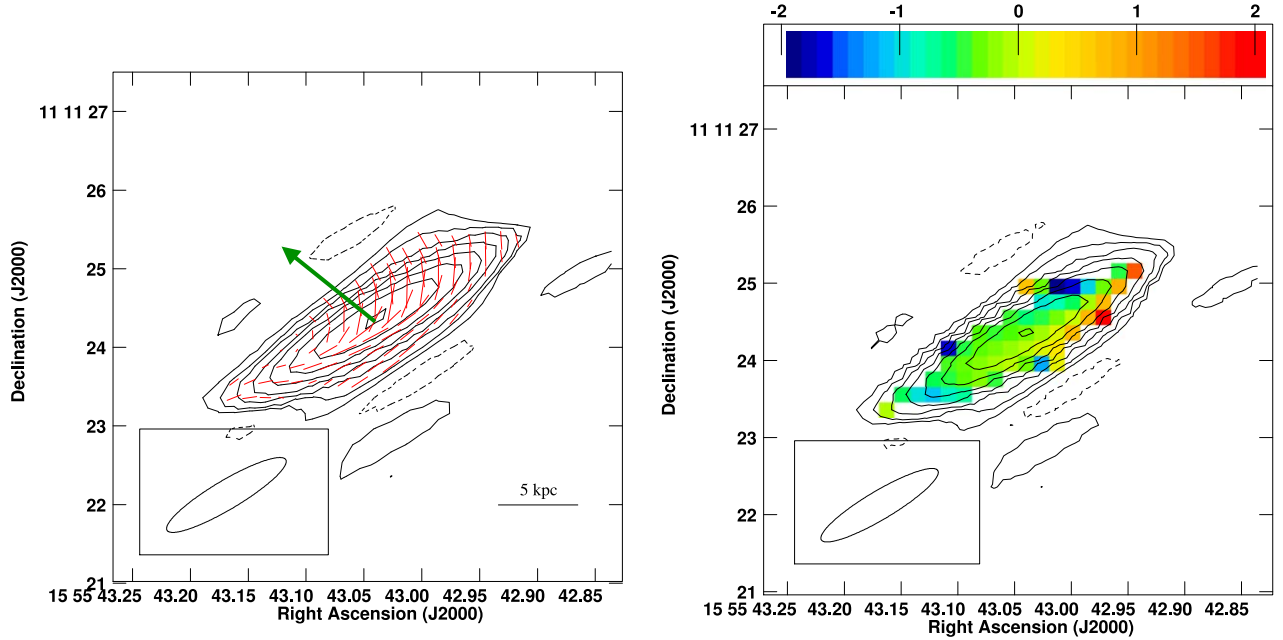


**Figure 7.** VLA 6 GHz contour image of BL Lac PG 1553+113 superimposed with (left) red polarized intensity vectors and (right) the in-band spectral index image. The VLBI jet direction is shown by the green arrow. The beam is  $1''.76 \times 0''.37$  with a PA of  $-59^\circ$ . The peak surface brightness,  $I_p$ , is  $0.31 \text{ Jy beam}^{-1}$  and the contour levels are  $I_p \times 10^{-2} \times (-0.7, 0.7, 1.4, 2.8, 5.6, 11.25, 22.5, 45, 90) \text{ Jy beam}^{-1}$ . A  $1''$  length of the vector corresponds to  $8.33 \text{ mJy beam}^{-1}$ .

picked up. The hot spots and other finer features are more clearly resolved in the P. Miller et al. (1993) image. The core EVPA is perpendicular to the local jet direction.

#### 4.2.7. PG 2308+098

This SSRQ (Figure 15) is a linear radio source with the western component at a slightly different angle than the eastern one (J. D. H. Pilkington & J. F. Scott 1965; G. Swarup et al. 1986; P. Miller et al. 1993; K. I. Kellermann et al. 1994). The parsec-scale 5 GHz VLBI image by A. Wang et al. (2023)

shows a tentative jet to the northwest. We find our VLA 6 GHz observations of this SSRQ match those of P. Miller et al. (1993) with more diffuse lobe emission being detected in the southeastern lobe and multiple jet knots and no clear hot spot seen in the northwestern jet. The southeastern hot spot shows typical B-field compression. The core EVPA is perpendicular to the jet direction.

Overall, we observe that most of the PG quasars have their core EVPAs perpendicular to their jet directions. Of the seven quasars presented in this paper, three have their core EVPAs perpendicular to their jet directions, and the other four show

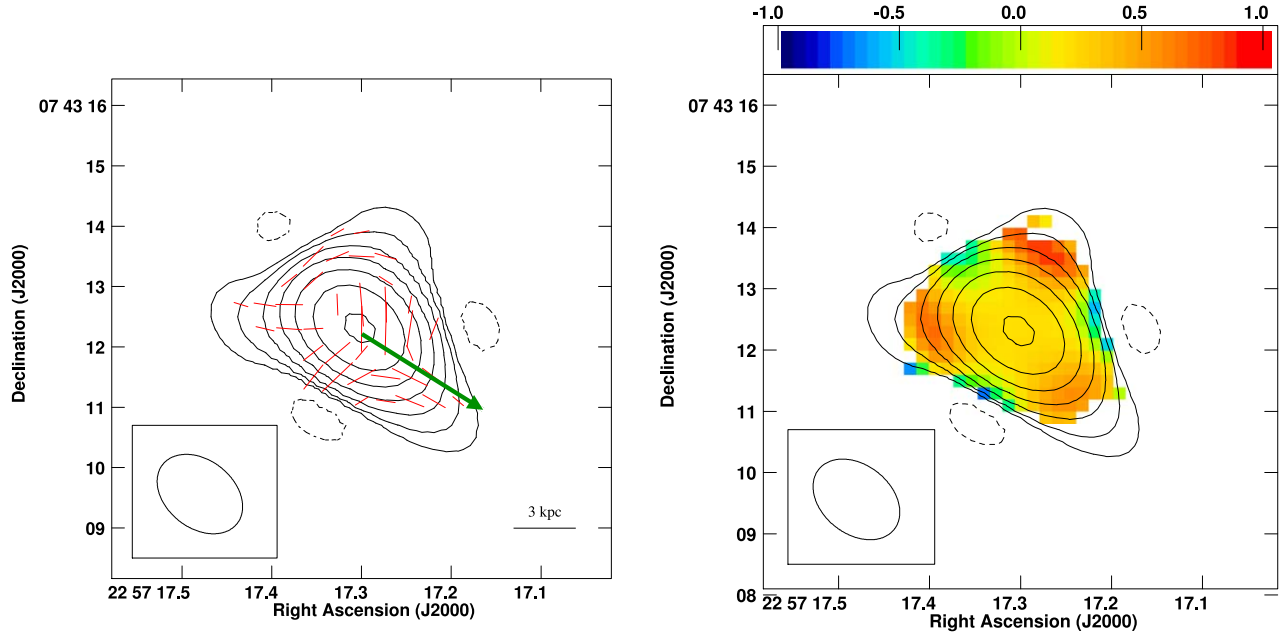


**Figure 8.** VLA 6 GHz contour image of BL Lac PG 2254+075 superimposed with (left) red polarized intensity vectors and (right) the in-band spectral index image. The VLBI jet direction is shown by the green arrow. The beam is  $1''.57 \times 1''.12$  with a PA of  $51^\circ$ . The peak surface brightness,  $I_p$ , is  $0.587 \text{ Jy beam}^{-1}$  and the contour levels are  $I_p \times 10^{-2} \times (-1.4, 1.4, 2.8, 5.6, 11.25, 22.5, 45, 90) \text{ Jy beam}^{-1}$ . A  $1''$  length of the vector corresponds to  $2.50 \text{ mJy beam}^{-1}$ .

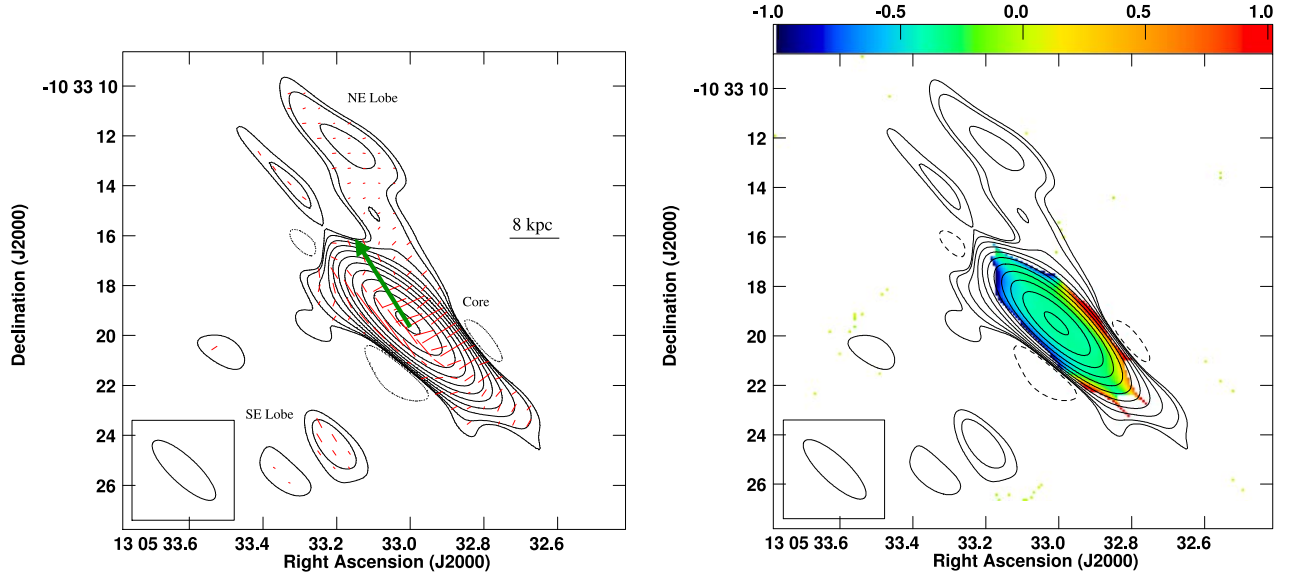


**Figure 9.** VLA 6 GHz contour image of quasar PG 1302-102 superimposed with (left) red polarized intensity vectors and (right) the in-band spectral index image. VLBI jet direction is shown by the green arrow. The beam is  $3''.33 \times 1''.06$  with a PA of  $47^\circ$ . The peak surface brightness,  $I_p$ , is  $0.68 \text{ Jy beam}^{-1}$  and the contour levels are  $I_p \times 10^{-2} \times (-0.12, 0.12, 0.18, 0.35, 0.7, 1.4, 2.8, 5.6, 11.25, 22.5, 45, 90) \text{ Jy beam}^{-1}$ . A  $1''$  length of the vector corresponds to  $6.25 \text{ mJy beam}^{-1}$ .

two mutually perpendicular polarization components in their cores. This could be consistent with optical depth effects as highlighted in D. C. Gabuzda (2003) and P. Kharb et al. (2008a). The kiloparsec-scale jet is also along the VLBI jet direction for all of the seven PG quasars presented here (See Table 5 and Figures 9–15).

### 5. Global Correlations

We have attempted to understand the interplay between accretion power, jet power, and the organization of B fields in kiloparsec-scale jets by examining correlations between various associated quantities discussed ahead. As the gamma-ray

luminosity and spectral energy distribution (SED) data are available for all the BL Lac objects, we have attempted to look for relations between them and radio polarization properties. We had previously looked at various global correlations for PG “blazar” subsamples using our own radio polarization data along with other multifrequency data from the literature in J. Baghel et al. (2023) and J. Baghel et al. (2024). Here, we look at new correlations using our observational data and other global properties for the entire PG “blazar” sample. In order to compare the two classes and the findings from our previous studies (J. Baghel et al. 2023; J. Baghel et al. 2024), we intended to examine and compare RL quasars and BL Lacs



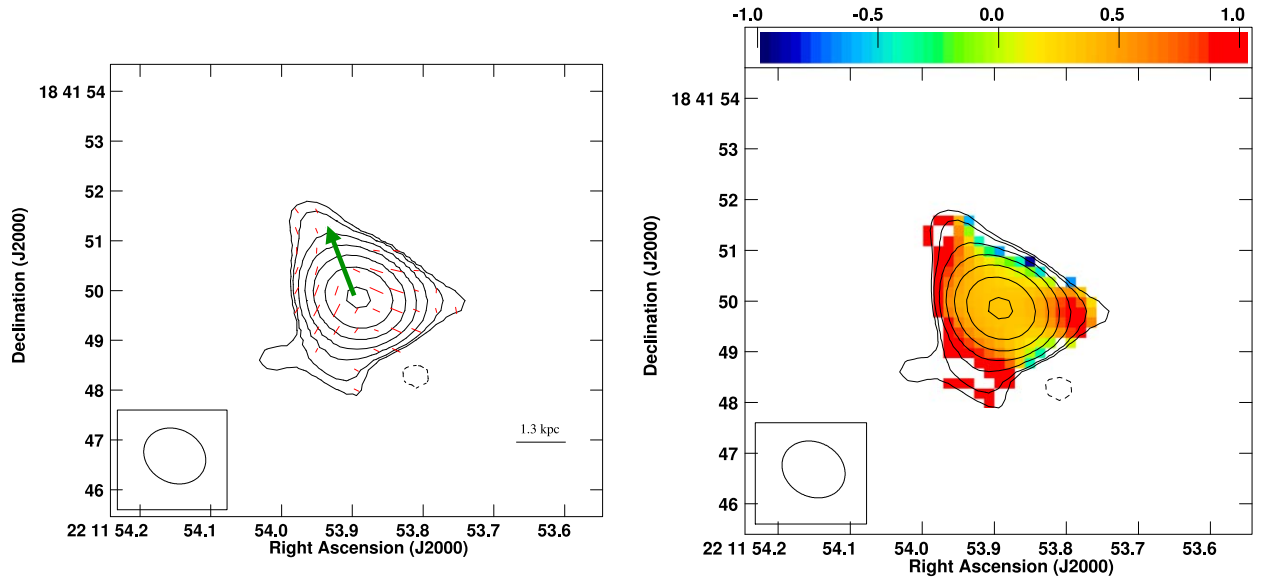


**Figure 10.** VLA 6 GHz contour image of quasar PG 2209+184 superimposed with (left) red polarized intensity vectors and (right) the in-band spectral index image. The beam is  $1''.29 \times 1''.07$  with a PA of  $62^\circ$ . The peak surface brightness,  $I_p$ , is  $0.103 \text{ Jy beam}^{-1}$  and the contour levels are  $I_p \times 10^{-2} \times (-1.9, 1.9, 2.8, 5.6, 11.25, 22.5, 45, 90) \text{ Jy beam}^{-1}$ . A  $1''$  length of the vector corresponds to  $1.25 \text{ mJy beam}^{-1}$ .

independently. We also note that we did find a marginally significant difference in the polarization distribution of the BL Lacs and quasars (KS test  $p$ -value = 0.0014). However, given the compact nature of the BL Lac radio emission, there is likely some jet/lobe emission contaminating the core emission, which could increase the “core” fractional polarization.

High energy luminosity ( $0.1\text{--}100 \text{ GeV}$ ;  $L_\gamma$ ), and synchrotron peak frequency  $\nu_s$  for the BL Lacs have been reported from FERMILPSC (the Fermi LAT 12 yr Point Source Catalog, 4FGL-DR3; S. Abdollahi et al. 2022) and the Fourth LAT AGN Catalog (4LAC-DR3; M. Ajello et al. 2022). Contrary to the BL Lacs, Fermi-LAT data were available for only one of the quasars, PG 1226+023. Quasars were therefore not considered for correlations with gamma-ray emission.

We have estimated the long-term time-averaged bulk radio jet kinetic power  $\bar{Q}$  for all blazars using the radio luminosity at 151 MHz as a surrogate for the luminosity of the radio lobes by using the relation given by B. Punsly et al. (2018),

$$\bar{Q} = 3.8 \times 10^{45} f L_{151}^{6/7} \text{ erg s}^{-1}$$

where  $L_{151}$  is radio luminosity at 151 MHz in units of  $10^{28} \text{ W Hz}^{-1} \text{ sr}^{-1}$  and  $f \approx 15$  (K. M. Blundell & S. Rawlings 2000). We obtained the  $L_{151}$  from the TGSS survey flux densities (H. T. Intema et al. 2017) using the relation  $L_{151} = [D_L^2 F_{151}] / [(1+z)^{(1+\alpha)}] \text{ W Hz}^{-1} \text{ sr}^{-1}$ ,<sup>11</sup> where we have used the typical average  $\alpha = -0.7$  for the extended emission. We report  $\bar{Q}$  without errors, as systematic uncertainties in the estimation methods dominate the statistical uncertainty in the data. Black hole masses  $M_{\text{BH}}$  and accretion rates  $\dot{M}$  have been reported by Z.-Z. Wu et al. (2009), J. Shangguan et al. (2018), S. W. Davis & A. Laor (2011), and B. Luo et al. (2013), who do not report errors for the same. Accretion rates for the quasars have been determined by S. W. Davis & A. Laor (2011) using thin accretion disk model spectral fits of optical lines. For the BAL

QSO PG 1004+130, an  $\eta = 0.1$  has been adopted by B. Luo et al. (2013) to compute the accretion rate. For the BL Lacs, we do not have a similarly determined estimate for accretion rates and hence we have not included them in the correlation tests. However, J. Shangguan et al. (2018) use the calibration of L. C. Ho & M. Kim (2015) to calculate  $M_{\text{BH}}$  that produces an uncertainty of  $\sim 0.3\text{--}0.4$  dex. The errors in  $L_\gamma$  and  $\nu_s$  are plotted as reported in the catalog or calculated from reported errors in the flux values.

The global parameters for the entire PG “blazar” sample are listed in Table 3. The fractional polarization, spectral index, and other observational quantities from our complete set of VLA observations are listed in two tables. Table 2 lists the observational parameters from the VLA images of PG BL Lacs and seven PG Quasars presented in this paper, and Table 4 lists the observational parameters of the nine PG quasars from J. Baghel et al. (2023), used in the correlations below.

With the complete sample of RL PG quasars (see Tables 2, 4, and 3), we find that the black hole masses  $M_{\text{BH}}$  are marginally correlated with the core fractional polarization  $\text{FP}_C$  (Kendall  $\tau$  test probability,  $p = 0.015$ ; left panel, Figure 16). This was also observed with the subset of the quasars presented in J. Baghel et al. (2023) and hence confirms this result for the PG RL quasars. However, we note that this correlation seems to be driven by the values for PG 1309+355 and weakens substantially when it is removed. With the entire quasar sample, we find that jet power  $\bar{Q}$  does not correlate with  $\text{FP}_C$  (Kendall  $\tau$  test  $p = 0.116$ ; right panel, Figure 16) as opposed to the weak correlation observed with the subsample presented in J. Baghel et al. (2023). Additionally, we find that the core spectral index  $\alpha$  is anti-correlated with  $\text{FP}_C$  ( $p$ -value = 0.0189; left panel, Figure 17). No such correlation with  $\alpha_C$  was found for BL Lac objects ( $p$ -value = 0.105).

We found a correlation between jet power  $\bar{Q}$  and  $\dot{M}$  in J. Baghel et al. (2023) for the PG quasars. In comparing the accretion power,  $\dot{M}c^2$ , to jet power, we find that in general  $\bar{Q} \sim 10^{-4} \dot{M}c^2$  for the FSRQs as in M. Sikora & M. C. Begelman (2013) and  $\bar{Q} \sim 10^{-2} \dot{M}c^2$  for the SSRQs (right panel, Figure 17).

<sup>11</sup> We note that there is no  $4\pi$  factor because of the anisotropic jet emission; e.g., see J. A. Peacock (1999).

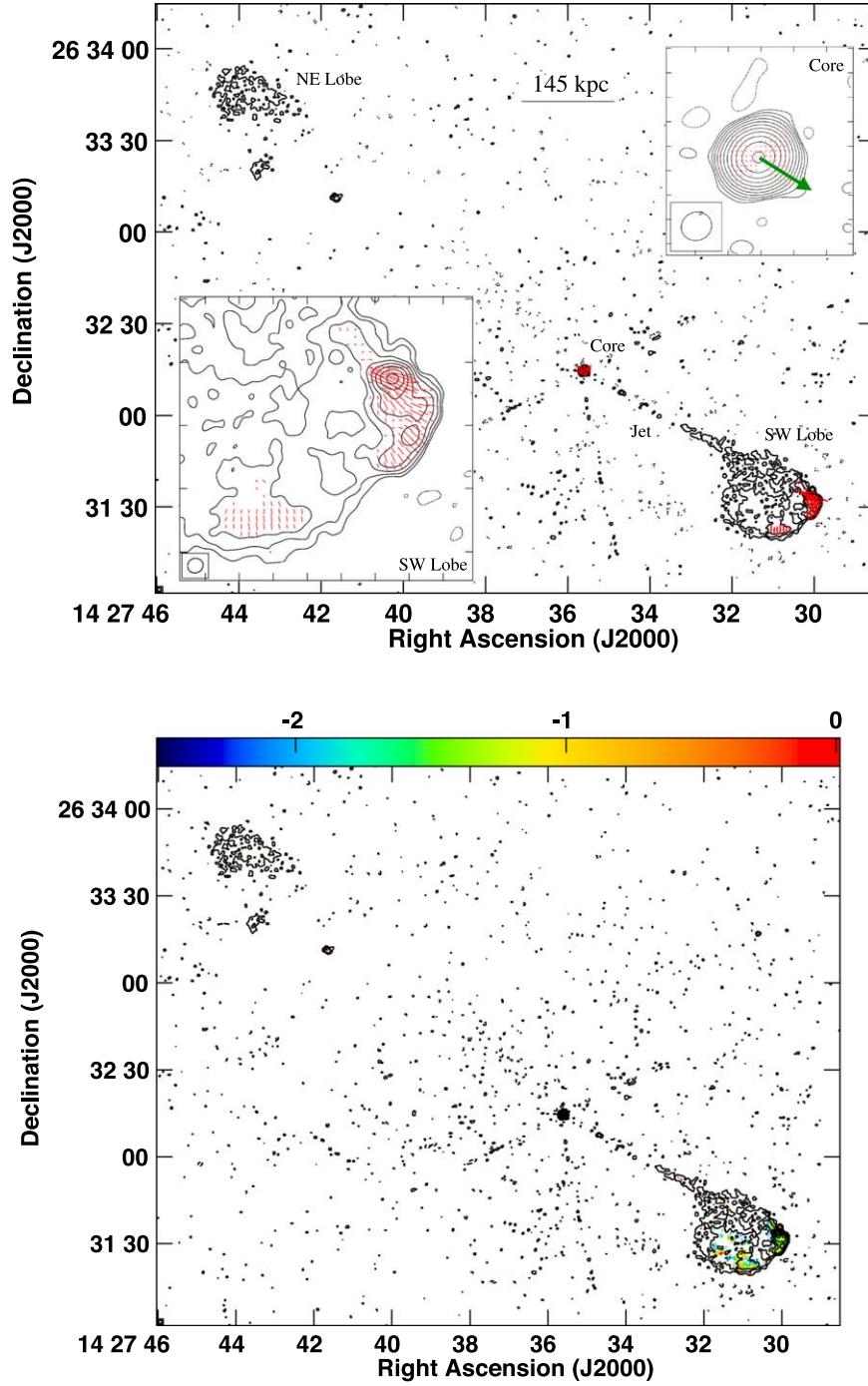


**Figure 11.** VLA 6 GHz contour image of quasar PG 1425+267 superimposed with (top) red polarized intensity vectors and (bottom) the in-band spectral index image. The insets show the core region and the southern hot-spot region. The beam is  $1''.26 \times 1''.15$  with a PA of  $-69^\circ$ . The peak surface brightness,  $I_p$ , is  $25.90 \text{ mJy beam}^{-1}$  and the contour levels are  $I_p \times 10^{-2} \times (-0.09, 0.09, 0.18, 0.35, 0.7, 1.4, 2.8, 5.6, 11.25, 22.5, 45, 90) \text{ Jy beam}^{-1}$ . A  $20''$  length of the vector corresponds to  $1 \text{ mJy beam}^{-1}$ .

For the case of the BL Lac objects, we find that, compared to the uGMRT 650 MHz  $\text{FP}_C$  data (J. Baghel et al. 2024), the correlation of  $\text{FP}_C$  with  $M_{\text{BH}}$  becomes insignificant ( $p$ -value = 0.170; left panel, Figure 18). We found no significant correlation between  $\text{FP}_C$  and  $\dot{Q}$  ( $p$ -value = 0.382; right panel, Figure 18). Correlations with gamma-ray luminosity ( $p$ -value = 0.061; left panel, Figure 19) and synchrotron peak luminosity ( $p$ -value = 0.061; right panel, Figure 19) are weakened compared to those reported in J. Baghel et al. (2024). These results are discussed below.

## 6. Discussion of the Complete PG Blazar Sample

Sources in the PG “blazar” sample show a wide variety of radio morphologies not easily classifiable into distinct FRI and FRII categories. We find that 7 of the 16 PG quasars show signatures of episodic or restarted AGN activity and disturbed morphology. These are PG 0007+106 (S. Silpa et al. 2021a; J. Baghel et al. 2023), PG 1302–102, PG 1004+130 (J. Baghel et al. 2023; S. Ghosh et al. 2023), PG 1100+772 (J. Baghel et al. 2023), PG 1103–006 (this work; J. Baghel et al. 2023),

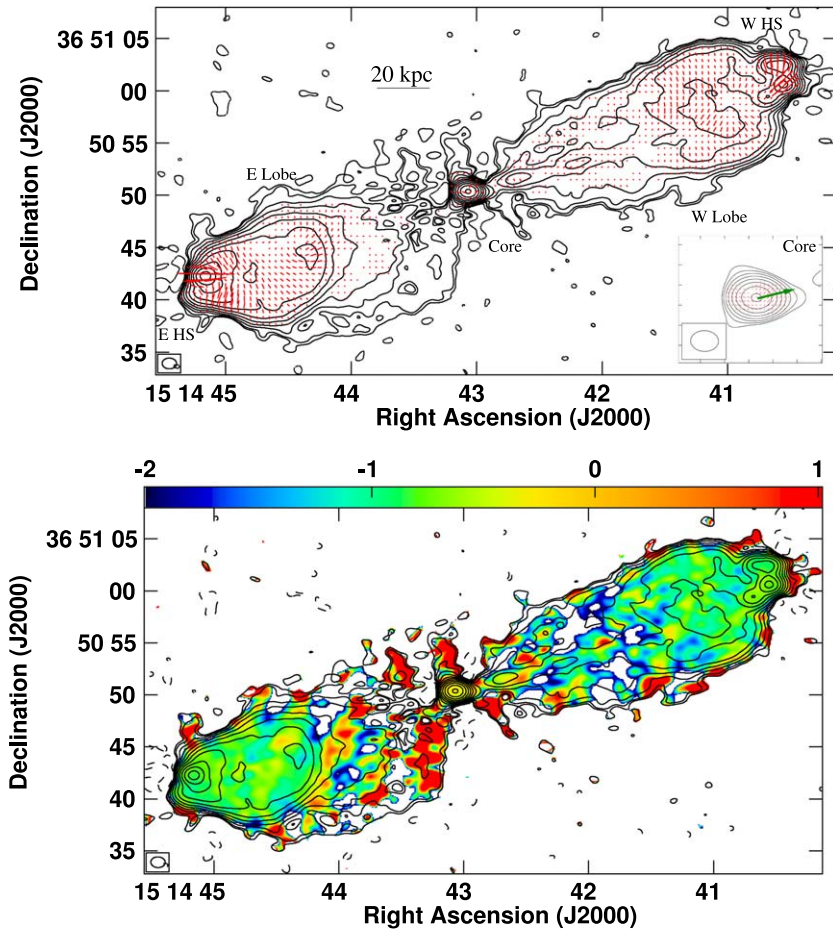


**Figure 12.** VLA 6 GHz contour image of quasar PG 1512+370 superimposed with (top) red polarized intensity vectors and (bottom) the in-band spectral index image. The inset shows the core region. The beam is  $1''.38 \times 1''.03$  with a PA of  $88^\circ$ . The peak surface brightness,  $I_p$ , is  $42.6 \text{ mJy beam}^{-1}$  and the contour levels are  $I_p \times 10^{-2} \times (-0.06, 0.06, 0.09, 0.18, 0.35, 0.7, 1.4, 2.8, 5.6, 11.25, 22.5, 45, 90) \text{ Jy beam}^{-1}$ . A  $1''$  length of the vector corresponds to  $1 \text{ mJy beam}^{-1}$ .

PG 1704+608 (J. Baghel et al. 2023), and PG 2308+098 (this work). The prevalence of diverse radio morphologies among the RL PG quasars contradicts the picture from the bright 3C sources, which typically consist of double radio sources (L. M. Mullin et al. 2008). The high number of distorted/hybrid/restarted radio structures in the PG quasars could be a consequence of the optical selection criteria of the PG sample that is biased toward luminous sources with high Eddington ratios (E. J. Hooper et al. 1996; A. Laor 2000; S. Jester et al. 2005), but which remains largely unbiased in terms of their radio properties. A more complex extended source population is also borne out by recent high-sensitivity low-frequency surveys with less restrictive selection effects than earlier studies, including candidate hybrid, restarted, and remnant sources (e.g., A. D. Kapińska et al. 2017; B. Mingo et al. 2019; N. Jurlin et al. 2021).

The PG quasars appear to show a greater diversity in their morphologies and total radio powers than the PG BL Lac objects. While the number of PG BL Lac objects is small, this finding is consistent with low-frequency LOFAR studies of larger radio galaxy samples (e.g., B. Mingo et al. 2019; V. H. Mahatma 2023). Two BL Lac objects, namely PG 0851+203 and PG 1418+546, show the presence of hot spots/jet bends in their uGMRT images (J. Baghel et al. 2024) that are consistent with an FR II morphology, which goes against the basic tenets of the simple Unified Scheme (C. M. Urry & P. Padovani 1995). These sources may have been misclassified

based on their optical spectra; a boosted optical continuum may have swamped the emission lines in these sources. These sources are also consistent with the blazar envelope scenario discussed ahead.

F. Massaro et al. (2020) have suggested that BL Lac objects' environs resemble those of FR0s, a core-dominated compact class of sources, more than those of FRIs. Two BL Lac objects, PG 1218+304 and PG 1553+113, do not exhibit obvious indications of extended emission, neither in their VLA images presented here nor in their uGMRT images presented in J. Baghel et al. (2024), and may resemble FR0s.

Our polarimetric data indicate overall that magnetic field structures present in the jets of PG quasars are aligned with the jets, while 4 of the 16 sources show some perpendicular magnetic field structures in their cores alone. We note that the inferred B fields are taken to be perpendicular to the EVPAs even for the core regions, in contrast to what we noted earlier in J. Baghel et al. (2023; see Footnote 8). Optical depth effects, as discussed in D. C. Gabuzda (2003), P. Kharb et al. (2008a), and others, can give rise to parallel/perpendicular EVPAs with respect to local jet directions.

In the PG BL Lac objects, however, the relationship observed in the magnetic field structures with their local parsec-scale jet directions (e.g., A. B. Pushkarev et al. 2023) is not present for the kiloparsec-scale jets (see also J. Baghel et al. 2024). We find complex EVPA structures suggesting multiple jet reorientations in five of the eight PG BL Lacs. This agrees



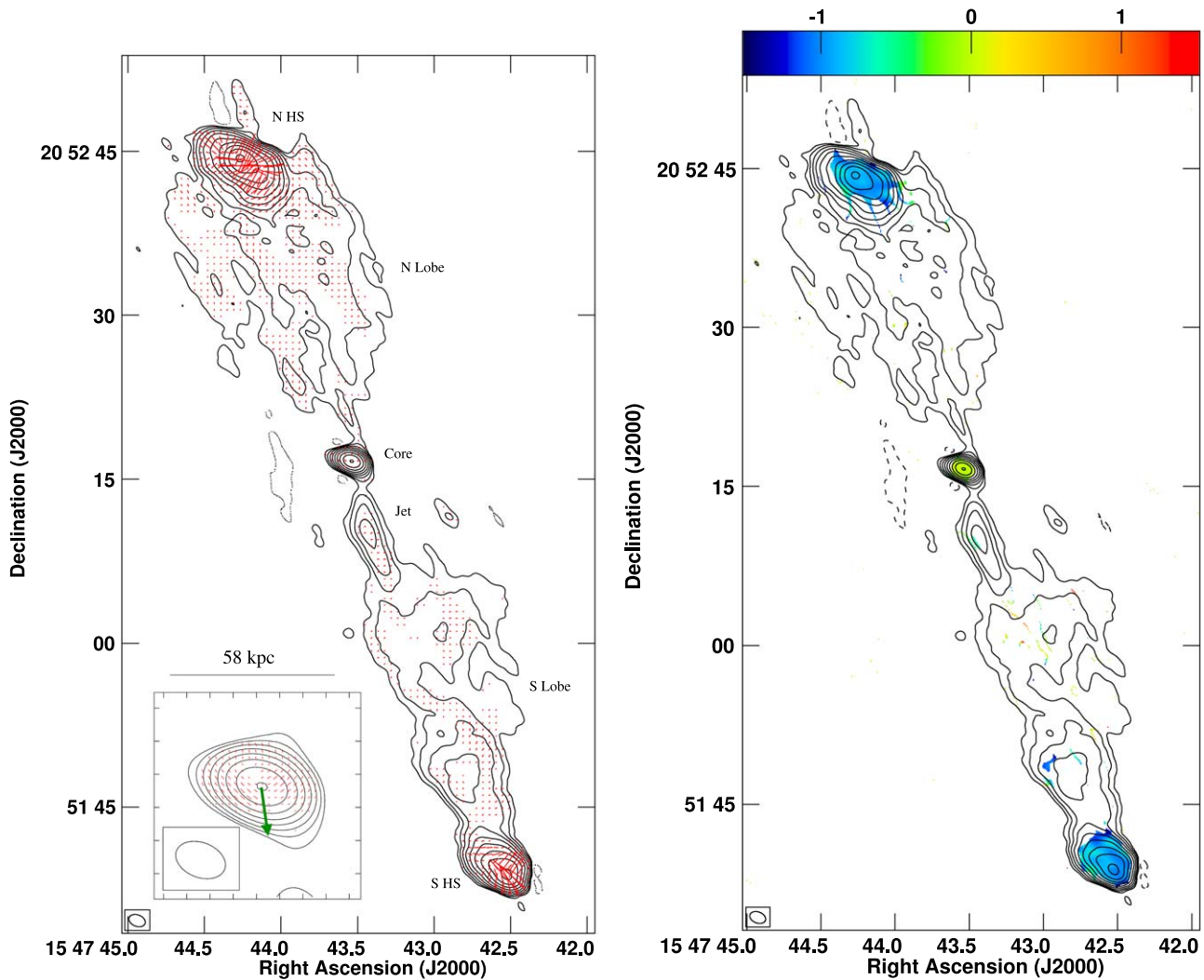


**Figure 13.** VLA 6 GHz contour image of quasar PG 1545+210 superimposed with (left) red polarized intensity vectors and (right) the in-band spectral index image. The inset shows the core region. The beam is  $1''.56 \times 1''.05$  with a PA of  $69^\circ$ . The peak surface brightness,  $I_p$ , is  $98.25 \text{ mJy beam}^{-1}$  and the contour levels are  $I_p \times 10^{-2} \times (-0.18, 0.18, 0.35, 0.7, 1.4, 2.8, 5.6, 11.25, 22.5, 45, 90) \text{ Jy beam}^{-1}$ . A  $5''$  length of the vector corresponds to  $8.33 \text{ mJy beam}^{-1}$ .

with previous studies, suggesting that their weaker jets interact with their environments and change direction (e.g., P. Kharb et al. 2010). Complex EVPA structures can also result from turbulent magnetic fields, as suggested by A. Marscher et al. (2017) and H. Zhang et al. (2020).

However, on the whole, there is a consistency in the observed magnetic field structures in the PG quasars and BL Lacs with those observed in FRI and FRII radio galaxies by A. H. Bridle & R. A. Perley (1984); that is, FRIs have their EVPAs either parallel to the local jet directions or parallel near the centers but perpendicular near the jet edges, while FRIIs have their EVPAs perpendicular to their local jet directions.

The polarimetric data further suggest that jet-medium interaction is likely to be playing an additional key role in the observed magnetic field structures. Jet-medium interaction can result in the creation of “shear” layers or jet “sheaths” (R. A. Laing 1996; P. Kharb et al. 2009) and also change the jet propagation direction in BL Lac objects. A clear spine-sheath magnetic field geometry is observed in the BL Lac object PG 1101+384 and possibly in PG 1424+240, combining the VLA and uGMRT (J. Baghel et al. 2024) polarimetric data. Changes in jet direction that are not resolved in our observations could result in a lowering of the degree of polarization on kiloparsec scales.

The hot spots of several quasars exhibit a steep spectral index, from  $-0.70 \pm 0.10$  up to  $-1.00 \pm 0.20$ , while the cores are typically flat spectrum. This could suggest that the hot spots in some sources are moving through plasma from a previous AGN activity episode (e.g., PG 1004+130 and 3C 219; D. A. Clarke et al. 1992 and S. Ghosh et al. 2023, respectively). Alternately, this may be an effect of the total radio power and/or redshift as discussed in J. Dennett-Thorpe et al. (1999). Higher-powered, more distant sources have steeper hot-spot spectra at a given emitting frequency; i.e., hot-spot spectra in more distant objects are detected at a higher emitting frequency. Moreover, the rest-frame spectra of quasar hot spots exhibit greater curvature than those of radio galaxies (J. Dennett-Thorpe et al. 1999). Greater synchrotron cooling in higher-redshift sources can also steepen the hot-spot spectra. However, these results have been questioned by S. Vaddi et al. (2019), who state that the luminosity–spectral index correlation is driven by the luminosity–redshift and the spectral index–redshift correlations and found no difference in the spectral indices of quasars and radio galaxies. Similarly, P. Kharb et al. (2008b) find steep hot-spot spectral indices in several FRII radio galaxies.

An association of greater black hole mass with greater jet power has been previously suggested by I. H. Whittam et al.



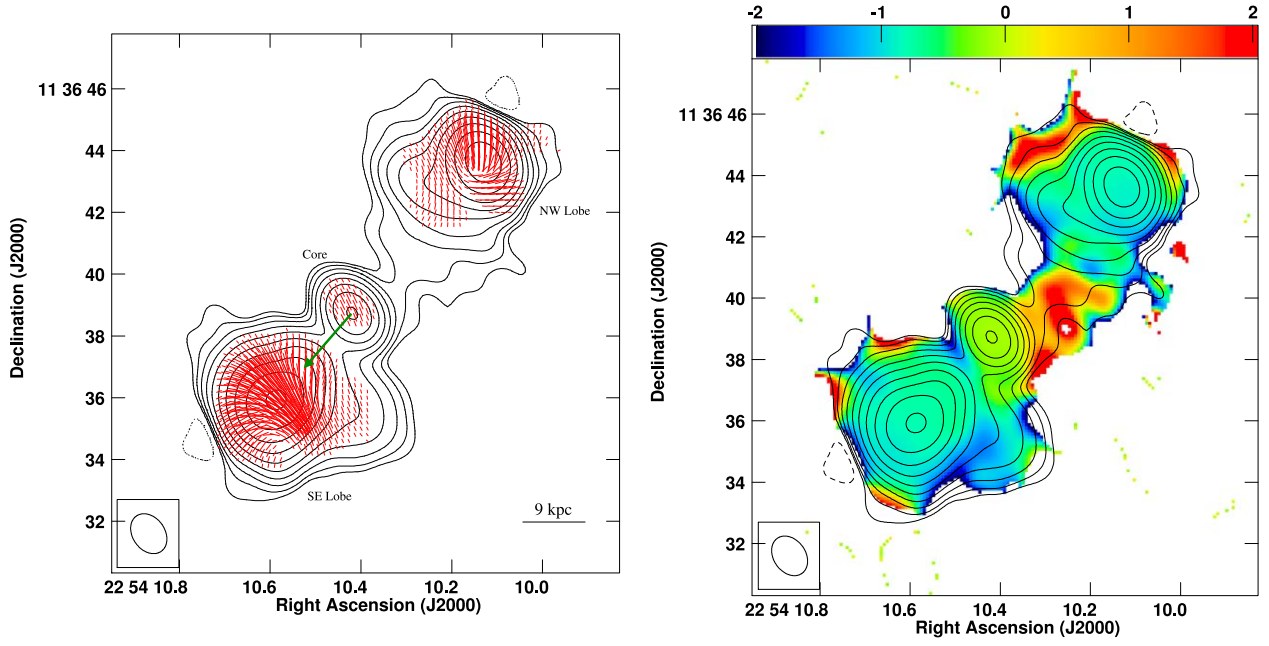


**Figure 14.** VLA 6 GHz contour image of quasar PG 2251+113 superimposed with (left) red polarized intensity vectors and (right) the in-band spectral index image. The beam is  $1''.40 \times 1''.04$  with a PA of  $35^\circ$ . The peak surface brightness,  $I_p$ , is  $0.134 \text{ Jy beam}^{-1}$  and the contour levels are  $I_p \times 10^{-2} \times (-0.18, 0.18, 0.35, 0.7, 1.4, 2.8, 5.6, 11.25, 22.5, 45, 90) \text{ Jy beam}^{-1}$ . A  $1''$  length of the vector corresponds to  $2.5 \text{ mJy beam}^{-1}$ .

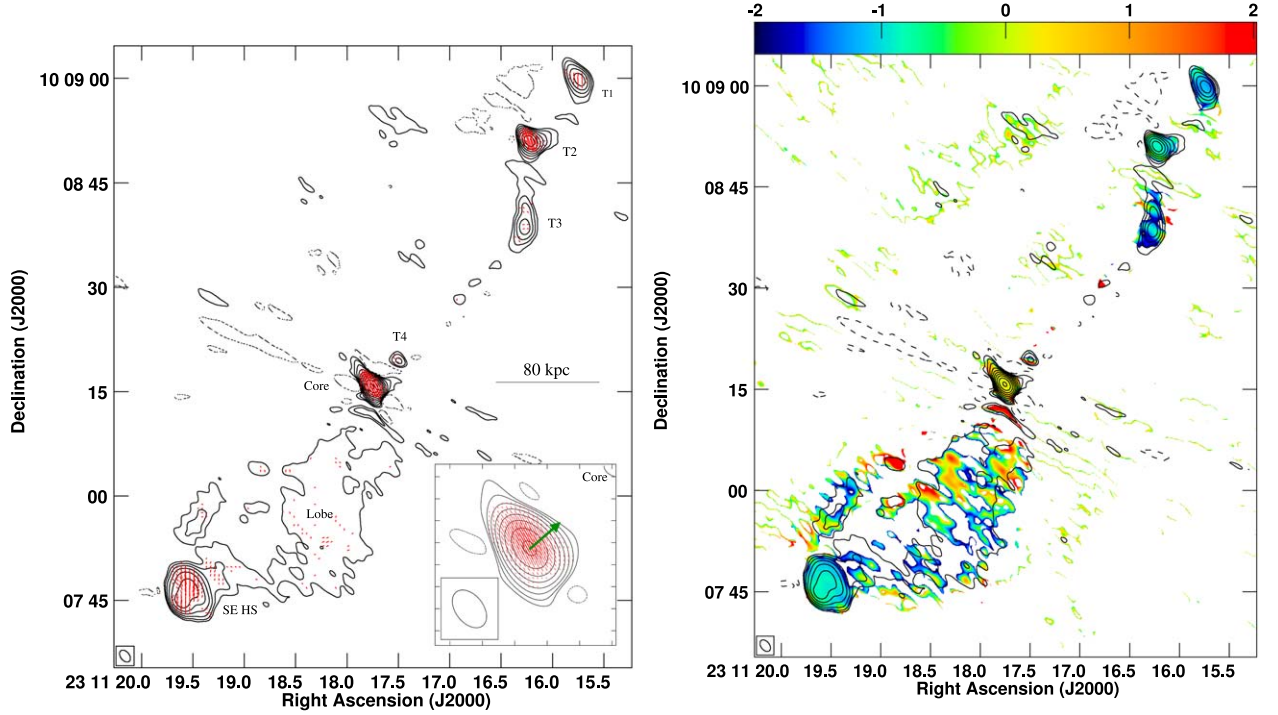


**Figure 15.** VLA 6 GHz contour image of quasar PG 2308+098 superimposed with (left) red polarized intensity vectors and (right) the in-band spectral index image. The inset shows the core region. The beam is  $1''.95 \times 1''.26$  with a PA of  $38^\circ$ . The peak surface brightness,  $I_p$ , is  $87.05 \text{ mJy beam}^{-1}$  and the contour levels are  $I_p \times 10^{-2} \times (-0.18, 0.18, 0.35, 0.7, 1.4, 2.8, 5.6, 11.25, 22.5, 45, 90) \text{ Jy beam}^{-1}$ . A  $5''$  length of the vector corresponds to  $2.5 \text{ mJy beam}^{-1}$ .

(2022). Instead, we find a potential correlation between the black hole masses with the core fractional polarization. While black hole masses are not statistically different between the PG quasars and PG BL Lac objects, we observe a correlation between black hole masses and core fractional polarization in the case of quasars alone. This may imply that more massive black holes tend to produce jets with more organized magnetic field structures in the case of quasars (e.g., J. Baghel et al.

2023). Alternately, well-organized, large-scale magnetic fields in the environments could promote the formation and early growth of black holes as proposed by M. C. Begelman & J. Silk (2023). The correlation is, however, marginal, and a larger sample is needed to confirm the same.

Environmental effects can explain the marginal anticorrelation observed between core spectral indices and core fractional polarization; the presence of thermal gas emitting free-free

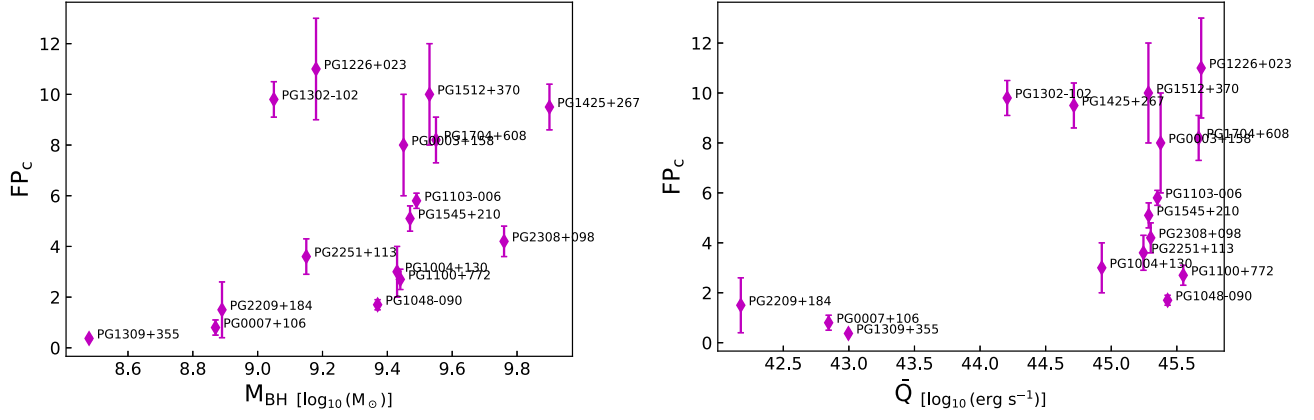


**Figure 16.** Core fractional polarization  $FP_C$  (percent) vs. log of BH masses ( $M_{BH}/M_{\odot}$ ) (left) and  $FP_C$  vs. log of jet power ( $\dot{Q}$  in  $\text{erg s}^{-1}$ ) (right) for the PG quasars.

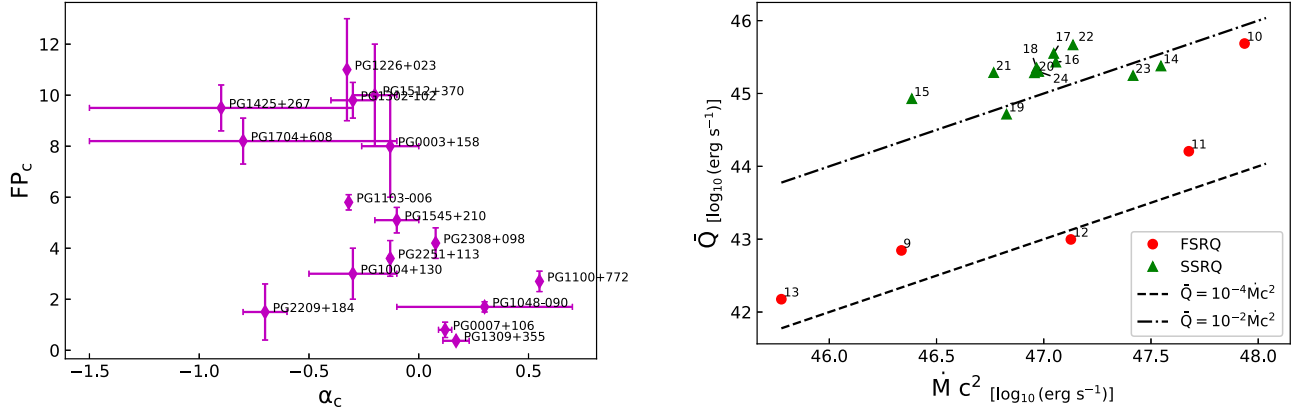


**Figure 17.** Core fractional polarization  $FP_C$  (percent) vs. core spectral index  $\alpha_c$  (left), and log of accretion power ( $\dot{M} c^2$  in  $\text{erg s}^{-1}$ ) vs. log of jet power ( $\dot{Q}$  in  $\text{erg s}^{-1}$ ) (right) for the PG quasars. The dashed lines shows  $\dot{Q} = 10^{-4} \dot{M} c^2$  and  $\dot{Q} = 10^{-2} \dot{M} c^2$ . The quasars are numbered by their S.No. in Table 3.

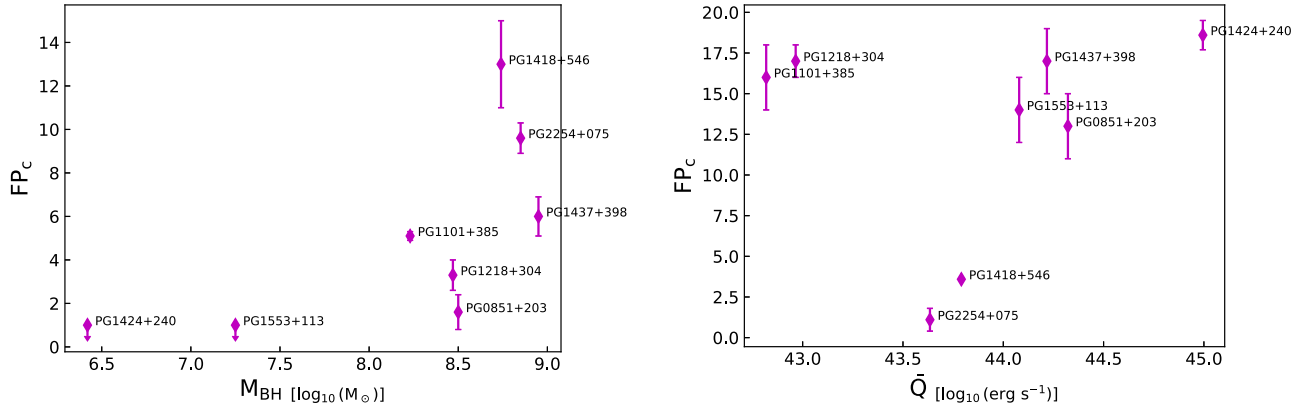


**Figure 18.** Core fractional polarization  $FP_C$  (percent) vs. log of BH masses ( $M_{BH}/M_{\odot}$ ) (left), and  $FP_C$  vs. log of jet power ( $\dot{Q}$  in  $\text{erg s}^{-1}$ ) (right) of the PG BL Lac objects.

emission along with synchrotron plasma at the jet bases could flatten the core spectral indices as well as reduce the core fractional polarization due to the presence of a greater Faraday-rotating medium. Another reason could be that we are sampling different regions in the source. A steep-spectrum core could be indicating that the core is observed at a frequency higher than its synchrotron peak, a flat-spectrum core would be near its synchrotron peak, and an inverted-spectrum core would be observed before the synchrotron peak. In the shock-in-jet scenario of E. Angelakis et al. (2016), the higher fractional polarization is observed from the shock-compressed compact

regions emitting near their synchrotron peaks. We did not find a correlation between core spectral indices and core fractional polarization for the BL Lacs, which could be resulting from the smaller number of BL Lacs in our sample, or jet component contamination to the core polarization. However, it could also mean that there is less gas at the jet base of BL Lac objects, or the shock-in-jet scenario, discussed above for the quasars, does not hold.

The association of total jet power with accretion power is also well known (S. Rawlings & R. Saunders 1991; G. Ghisellini et al. 2010; B. Punsly 2011; M. Sikora &

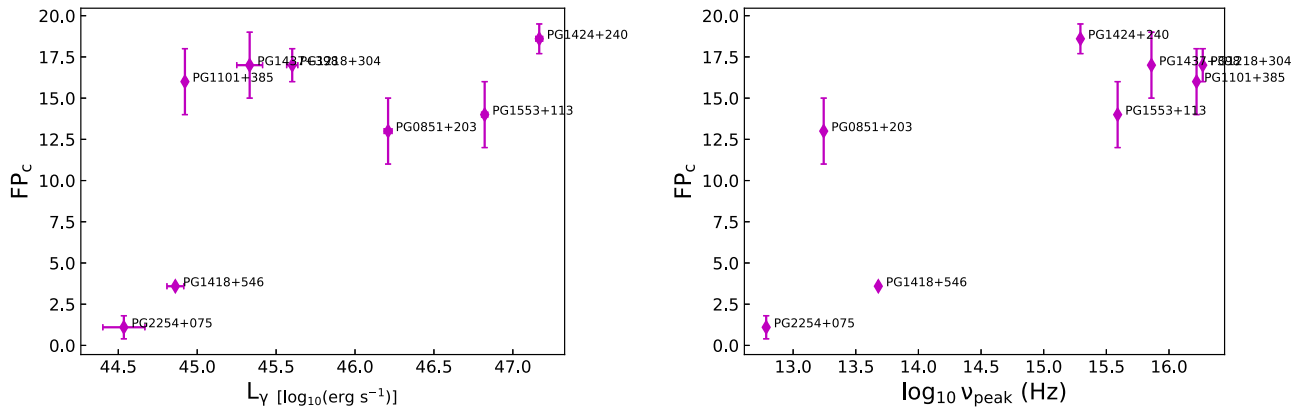


**Figure 19.** Core fractional polarization  $FP_C$  (percent) vs. log of gamma-ray luminosity  $L_\gamma$  (erg s $^{-1}$ ) (left), and  $FP_C$  vs. log of synchrotron peak frequency  $\nu_{\text{peak}}$  (Hz) (right) of the PG BL Lac objects.

M. C. Begelman 2013); the PG FSRQs follow the general relation of quasars with  $\dot{Q} \sim 10^{-4} \dot{M} c^2$  as noted in M. Sikora & M. C. Begelman (2013), and the SSRQs closely follow the relation  $\dot{Q} \sim 10^{-2} \dot{M} c^2$  with a higher jet production efficiency. This range in jet production efficiency and the tight correlations may be due to the dominance of the Blandford–Znajek mechanism in the formation of these jets (R. D. Blandford & R. L. Znajek 1977).

The blazar envelope scenario (E. T. Meyer et al. 2011; M. Keenan et al. 2021) suggests that the FRI and FRII jets have two different structures with the FRIs comprising structured jets with slow intrinsic speeds and inefficient accretion disks, and FRIIs having single Lorentz factor high-speed jets and efficient accretion disks. This differentiation in the jet velocities would then also explain the differences in the magnetic field structures along the jets in FRI and FRII (consistent with BL Lacs and quasars, respectively), even if they have similar black hole spins with either tightly or loosely wound helical magnetic fields resulting from a lower or higher jet velocity (D. C. Gabuzda 2015).

The PG quasar jets also seem to be characterized by perpendicular EVPAs with respect to jet direction going from parsec to kiloparsec scales, possibly suggesting single bulk velocity jets with no substructures. The PG BL Lacs, however, show a marked discontinuity in their parsec-scale to kiloparsec-scale EVPAs-to-jet-direction behavior (J. Baghel et al. 2024). This could relate to internal depolarization occurring inside the structured, possibly spine-sheath-like jets (e.g., PG 1101+384 and PG 1424+240), as well as external depolarization occurring by the jet’s interaction with the surrounding medium. We also find that the LSP BL Lacs among the PG BL Lacs are the ones displaying “strong” jet characteristics in accordance with the blazar envelope scenario. The PG BL Lacs also show a smaller range in their jet powers compared to the PG quasars, again hinting at the BL Lacs as a class being “weak” jet sources with inefficient accretion disks.

Under the magnetic flux paradigm (S. van Velzen & H. Falcke 2013; A. Tchekhovskoy 2015; M. Sikora 2016), jets are launched by the magnetically arrested accretion disks (MADs) due to the accumulation of large net magnetic flux. Fluctuating accretion flows can deposit sudden large amounts of flux onto the black hole, leading to intermittent jet production. This mechanism, being scale invariant, is also valid for X-ray binary sources. In such a case, FRI jets can be taken as the counterparts of steady-state X-ray binary jets with

weak but persistent radio emission, whereas FRII jets would be counterparts to the flaring jet state of X-ray binaries in the hard-to-soft state transition of their accretion disks. In more sensitive recent studies that go down to milli-Jansky flux densities, FRIs are found to be more common in the local Universe ( $z \leq 0.15$ ), and there is evidence that FRIIs have accretion disks that transition from high to low accretion regimes (P. Grandi et al. 2021).

The PG quasars show multiple recurrent patchy knots and disturbed diffuse structures in both their total intensity and polarization structures that might indicate quasi-periodic jet modulation seen in an unstable accretion disk (e.g., as noted by L. E. H. Godfrey et al. 2012). Recurrent activity is also found to be more prevalent in LERG FRIIs than in HERG FRIIs where episodic spikes in the accretion rate are expected (V. H. Mahatma 2023). Hybrid morphology sources could be the result of restarted activity combined with orientation effects on intrinsic FRII sources (J. J. Harwood et al. 2020; S. Ghosh et al. 2023). L. Saripalli et al. (2012) show that about 33% of FRIIs and 13% of FRIs show evidence of restarted activity in their sample, whereas more recently N. Jurlin et al. (2020) have found the incidence to be between 13% and 15% in their LOFAR study, with restarted double-double radio sources being commonplace. While the greater incidence of such restarted and remnant sources within the PG quasars compared to the BL Lacs might be attributable to projection effects, these differences persist even when comparing FSRQs and BL Lacs, which both have smaller viewing angles.

The blazar envelope picture (E. T. Meyer et al. 2011; M. Keenan et al. 2021) can coexist with the scenario suggested by the MAD mechanism of jet launching under the magnetic flux paradigm (S. van Velzen & H. Falcke 2013; A. Tchekhovskoy 2015; M. Sikora 2016). The FRII sources will be the ones with the radiatively inefficient geometrically thick accretion flow transitioning in a turbulent manner to a radiatively efficient geometrically thin accretion flow with the launch of flaring jets taking a period of  $10^4$ – $10^7$  yr. These flaring jets would then also be associated with a perturbed accretion disk, which would lead to restarted activity and changes in jet direction and will also have higher bulk velocities (R. P. Fender et al. 2004; N. D. Kylafis et al. 2012; M. Sikora & A. A. Zdziarski 2023). Our results agree with this combined scenario.

## 7. Conclusions

We present polarization-sensitive 6 GHz VLA images of seven quasars and eight BL Lac objects belonging to the Palomar-Green sample. This paper completes the polarization study of the PG “blazar” sample presented previously in J. Baghel et al. (2023) and J. Baghel et al. (2024). We summarize below our main conclusions from the entire sample.

1. The radio morphology of the PG quasars is more diverse compared to the brighter 3C sources that show double FR II-like radio lobes in the literature. Morphological signatures of restarted activity like changes in jet propagation directions or changes in spectral indices are present in 7 out of 16 PG quasars. The PG BL Lacs, in comparison, are less diverse in their radio morphologies. The quasi-periodic jet knots, jet precession, and restarted activity in quasars might be indicative of an unstable accretion disk, agreeing with a possible evolutionary scenario wherein they are undergoing an accretion mode transition.
2. The radio morphology of the BL Lac objects is typically core-halo type or FR I like in the case of PG 1424+240 and PG 1437+398, with the main exceptions being the LSP BL Lacs PG 0851+203 and PG 1418+546. These display radio morphology and polarization characteristics of “strong” jet sources consistent with the “blazar envelope scenario.” The PG BL Lacs also show a smaller range of total radio power compared to the PG quasars, consistent with them being driven by inefficient accretion disks.
3. We detect kiloparsec-scale polarization with the VLA in all the blazars with fractional polarization ranging from  $0.8\% \pm 0.3\%$  to  $37\% \pm 6\%$  in their cores and jets/lobes. In the PG quasars, the polarization structures are consistent with jets primarily displaying aligned magnetic fields along the jets and transverse magnetic fields in the terminal hot spots. The magnetic field structures are more complex in the BL Lac objects, suggestive of smaller substructures with distinct magnetic field orientations that are not resolved in our VLA observations.
4. The kiloparsec-scale magnetic field orientation in the quasar cores is parallel to their VLBI jet directions, which in most cases is the same as their kiloparsec-scale jet directions. In the case of most BL Lacs, the kiloparsec-scale core magnetic field orientations show no correlation to the VLBI jet directions. This might indicate multiple jet reorientations for the PG BL Lac objects.
5. The hot spots of several quasars exhibit a steep spectral index, from  $-0.7 \pm 0.1$  up to  $-1.0 \pm 0.2$ , while the cores are typically flat spectrum. This could be consistent with episodic AGN activity, spectral aging due to synchrotron cooling, or the observed relations between hot-spot spectra and total radio power. An anticorrelation between the core spectral indices and core fractional polarization

could be consistent with the presence of thermal gas along with synchrotron plasma at the jet bases and elsewhere. Environmental effects are also reflected in spine-sheath-like magnetic field structures that are observed in a couple of PG blazars.

6. For the PG quasars, we find that the black hole masses are marginally correlated with the kiloparsec-scale core fractional polarization. This may be driven by massive black holes producing jets with highly ordered magnetic fields or environments with highly ordered magnetic fields producing more massive black holes. For the PG quasars, jet power is positively correlated with the accretion power with high jet production efficiencies. This suggests the predominance of the Blandford–Znajek mechanism in the production of these jets.

Overall, we find that the PG “blazar” sample provides a rich set of radio polarimetric and spectral index data that elucidate the nature of radio jets in an optically selected sample. The optical selection criteria bias the sources to have relatively high accretion rates without a corresponding bias in the radio emission produced in these sources. This results in a diverse set of morphologies and magnetic field structures in jets of radio-loud AGN.

## Acknowledgments

We thank the referee for their helpful and insightful suggestions that have improved this paper significantly. J.B., P.K., and S.G. acknowledge the support of the Department of Atomic Energy, Government of India, under the project 12-R&D-TFR-5.02-0700. L.C.H. was supported by the National Science Foundation of China (11991052, 12233001), the National Key R&D Program of China (2022YFF0503401), and the China Manned Space Project (CMS-CSST-2021-A04, CMS-CSST-2021-A06). C.M.H. acknowledges funding from a United Kingdom Research and Innovation grant (code: MR/V022830/1). S.S. acknowledges financial support from Millennium Nucleus NCN23\\_002 (TITANs) and Comité Mixto ESO-Chile. The National Radio Astronomy Observatory is a facility of the National Science Foundation operated under cooperative agreement by Associated Universities, Inc. This research has made use of the NASA/IPAC Extragalactic Database (NED), which is operated by the Jet Propulsion Laboratory, California Institute of Technology, under contract with the National Aeronautics and Space Administration.

## Appendix A Tables

Below are the tables for the VLBI jet directions for PG blazars (Table 5) and the observational details of PG blazars presented in this paper (Table 6).



**Table 5**  
VLBI Jet Directions of the PG Blazars

Source	VLBI Jet PA	References	EVPA Core (15 GHz VLBA)	EVPA Core (6 GHz VLA)
BL Lacs				
PG 0851+203	−109°	(1)	⊥	⊥
PG 1101+385	−31°	(1)	oblique/ ∥	oblique/⊥
PG 1218+304	+92°	(1)	...	oblique/⊥
PG 1418+546	+126°	(1)	oblique	⊥
PG 1424+240	+145°	(1)	∥	∥
PG 1437+398	+56°	(1)	...	...
PG 1553+113	+51°	(1)	∥	oblique/⊥
PG 2254+075	−122°	(1)	∥/oblique	oblique
Quasars: FSRQ				
PG 0007+106	−115°	(1)	oblique/⊥	⊥
PG 1226+023	−130°	(1)	⊥	⊥
PG 1302+102	+32°	(1)	⊥	⊥
PG 1309+355	+130°	(1)	...	⊥
PG 2209+184	+21°	(1)	...	⊥
Quasars: SSRQ				
PG 0003+158	+116°	(1)	...	⊥
PG 1004+130	~+135°	(2)	...	⊥
PG 1048-090	−20°	(1)	...	⊥
PG 1100+772	+94°	(1)	...	⊥
PG 1103-006	−30°	(1)	...	⊥
PG 1425+267	−122°	(1)	...	⊥
PG 1512+370	−76°	(1)	...	⊥
PG 1545+210	−172°	(1)	...	⊥
PG 1704+608	... <sup>a</sup>	(2)	...	⊥ <sup>b</sup>
PG 2251+113	+139°	(1)	...	⊥
PG 2308+098	−49°	(1)	...	⊥

**Notes.** Column (1): PG source names. Column (2): mean VLBI jet position angle. Column (3): references for mean VLBI jet position angle. Column (4): EVPA in core (from stacked 15 GHz VLBA data; A. B. Pushkarev et al. 2023) versus VLBI jet PA. Column (5): EVPA in core (6 GHz VLA; this work and J. Baghel et al. 2023) versus VLBI jet PA. “...” refers to cases where the 15 GHz VLBI core EVPA was not available.

<sup>a</sup> Unresolved in VLBA 5 GHz image by Wang et al. (2023).

<sup>b</sup> Perpendicular to kiloparsec-scale jet direction.

**References.** (1) A. V. Plavin et al. (2022); (2) A. Wang et al. (2023), VLBA at 5 GHz.

**Table 6**  
Observational Details of PG “Blazars” Presented in This Paper

Name	Observation Date	Array Config	Flux Calibrator	Phase Calibrator	Leakage Calibrator	Angle Calibrator
PG 0851+203	19-06-2023	BnA	3C 286	J0842+1835	OQ 208	3C 286
PG 1101+384	22-06-2023	BnA → A	3C 286	J1130+3815	OQ 208	3C 286
PG 1218+304	14-04-2023	B	3C 286	J1221+2813	OQ 208	3C 286
PG 1418+546	18-06-2023	BnA	3C 286	J1349+5341	OQ 208	3C 286
PG 1424+240	20-06-2023	BnA	3C 286	J1436+2321	OQ 208	3C 286
PG 1437+398	21-06-2023	BnA → A	3C 286	J1416+3444	OQ 208	3C 286
PG 1553+113	20-06-2023	BnA → A	3C 286	J1608+1029	OQ 208	3C 286
PG 2254+075	16-04-2023	B	3C 138	J2241+0953	3C 84	3C 138
PG 1302+102	13-05-2023	B	3C 286	J1246+0730	OQ 208	3C 286
PG 2209+184	24-03-2023	B	3C 138	J2139+1423	3C 84	3C 138
PG 1425+267	15-01-2023	B	3C 286	J1407+2827	OQ 208	3C 286
PG 1512+370	28-04-2023	B	3C 286	J1602+3326	OQ 208	3C 286
PG 1545+210	28-04-2023	B	3C 286	J1513+2338	OQ 208	3C 286
PG 2251+113	10-03-2023	B	3C 138	J2241+0953	3C 84	3C 138
PG 2308+098	10-03-2023	B	3C 138	J2241+0953	3C 84	3C 138

**Note.** Column (1): PG names of sources. Column (2): observation date. Column (3): array configuration. Column (4): flux calibrator. Column (5): phase calibrator. Column (6): polarization leakage calibrator. Column (7): polarization angle calibrator.

## Appendix B Notes on Quasars

### B.1. PG 1302-102

J. B. Hutchings & S. G. Neff (1992) and J. N. Bahcall et al. (1995) presented optical images that show a smooth elliptical host galaxy with a small eccentricity for PG 1302-102. These optical images also show a  $0''.5$  wide object  $2''$  to the north, and also a bright feature  $0''.8$  to the west of the nucleus. S. Veilleux et al. (2009) and M. Kim et al. (2017) use the Spitzer and Hubble Space Telescope (HST) images, respectively, to argue that the host morphology is not strictly elliptical but ambiguous. There is no correlation between the optical and radio structures. Instead, the radio lobes appear to be pushed back from the inner optical knot. The hybrid optical luminosity profile of the mildly disturbed host elliptical, along with the linear shape of the nearest optical feature at  $0''.8$  (a possible small merging companion) and the relatively undisturbed extended radio emission, suggests this to be a minor merger with the companion spiraling into the primary elliptical galaxy for some time (J. B. Hutchings & S. G. Neff 1992). HST images of Y. Zhao et al. (2021) also detect a possible remnant from the merger as extended emission to the north. There is marginal evidence for PG 1302-102 being in a galaxy cluster (M. G. Yates et al. 1989; H. K. C. Yee & E. Ellingson 1993).

### B.2. PG 2209+184

PG 2209+184 is very compact and resides in a spherical galaxy (F. Zwicky & M. A. Zwicky 1971). It also shows night-to-night optical variability (M. Jang & H. R. Miller 1995). L. Villafañe et al. (2022) have modeled the velocity-resolved reverberation response of the  $H\beta$  broad emission line for PG 2209+184 and found a mean BLR radius of 15.2 light days and BLR opening and inclination angles of  $29^\circ.1$  and  $30^\circ.1$ , respectively, indicating the BLR is a thick disk slightly inclined to the line of sight.

### B.3. PG 1425+267

A. Laor et al. (1997) found PG 1425+267 to be weaker in soft X-rays compared to other radio-loud quasars. It is hosted by a bright elliptical galaxy that has three companions within  $10''$ , hinting at a possible interaction (I. Márquez et al. 2001). It has associated absorption at  $z = 0.3605$  and  $0.3643$  (J. Bechtold et al. 2002). It shows intranight optical variability of  $\sim 4$  hr (C. S. Stalin et al. 2005). An emission line cloud up to  $3''$  from the nucleus has been detected (T. A. Boroson & J. B. Oke 1984; A. Stockton & J. W. MacKenty 1987). The [O III] emission extends into two opposing extensions to the east and west (A. Stockton & J. W. MacKenty 1983).

### B.4. PG 1512+370

PG 1512+370 was first identified with an optical faint galaxy by E. T. Olsen (1970). J. N. Bahcall et al. (1993) noted a possible association with C IV absorption. Optical observations by A. Stockton (1978) and others show another galaxy with the same redshift in the field, with J. Bergeron & F. Durret (1987) finding a tentative continuum bridge linking the galaxy and the quasar. E. Ellingson et al. (1994) note that there are two other galaxies lying close to the quasar ( $<60$  kpc), but it is uncertain if they are cospatial with the quasar or foreground/background sources. Hence, the quasar may lie in a small group of galaxies

(H. K. C. Yee & R. F. Green 1987; E. Ellingson et al. 1994). PG 1512+370 also has an extremely luminous extended emission line region (EELR) extending up to 200 kpc (A. Stockton & J. W. MacKenty 1987; D. L. Block & A. Stockton 1991), exceptionally so among quasars at  $z \lesssim 0.5$ . C. S. Crawford & C. Vanderriest (2000) carried out optical integral field spectroscopy of the EELR around PG 1512+370 using the ARGUS instrument on the Canada–France–Hawaii Telescope (CFHT) and found two off-nuclear [O III] clouds to the east and northwest of the quasar. The distribution of the optical continuum and line emission were uncorrelated, but both seem to be embedded in a low-level diffuse emission. Additionally, the clouds had their most blueshifted regions spatially coinciding with the radio source axis, though any relationship between the regions is not obvious given the difference in the extent of the two emissions with the radio lying on a much larger scale. This [O III] region also reveals filamentary structure in its HST image (A. Stockton et al. 2002). In hard X-rays, M. Akiyama et al. (2003) found a source coincident with PG 1512+370 using the High-Resolution Imager (HRI) of ROSAT.

### B.5. PG 1545+210

The optical counterpart for PG 1545+210 was found by J. D. Wyndham (1966), and there have been several investigations into the luminous elliptical host galaxy and environment of PG 1545+210 (G. Neugebauer et al. 1995; J. N. Bahcall et al. 1997). Optical continuum and emission line images by G. M. van Heerde (1988) and R. Hes et al. (1996) show two companion objects  $19''$  to the southeast ( $PA = 117^\circ$ ) and  $12''$  toward the west ( $PA = 276^\circ$ ) with faint trails of [O III] emission linking them to the quasar core. The [O III] line emission is mostly concentrated toward the western companion, extending from the southeast of the quasar, making it asymmetrical. C. S. Crawford & C. Vanderriest (2000) have carried out optical integral field spectroscopy of the EELR in PG 1545+210 using the ARGUS instrument on the CFHT. A. Stockton (1982) had earlier identified a closer companion  $2''.7$  to the northwest in their continuum image, with line emission confirming that it is at the same redshift and associated with the quasar. J. B. Hutchings et al. (1988), using optical contour plots, after subtracting the quasar light, identified several compact objects or knots, specifically one at  $1''.3$  toward the northwest and another at  $3''$  toward the south in the asymmetrical host galaxy, further indicating this to be a merging source. HST imaging by J. N. Bahcall et al. (1995, 1997) and by M. Kim et al. (2017) further confirms the companion at  $2''.7$  to be another elliptical galaxy. PG 1545+210 is located toward the edges of a rich galaxy cluster, as it lies  $7'$  away from the center and at the same redshift as a compact Zwicky cluster 1545.1+2104 (Oemler et al. 1972; H. K. C. Yee & R. F. Green 1984).

### B.6. PG 2251+113

PG 2251+113 is bright in infrared (J. B. Hutchings & S. G. Neff 1992) and has an extended [O III] emission region similar in size and spatially coincident with the radio source (A. Stockton & J. W. MacKenty 1987; J. B. Hutchings & D. Crampton 1990; C. S. Crawford & C. Vanderriest 2000). The gas exhibiting the strongest blueshift is found at the same location as the southern radio hot spot along with being slightly more

ionized, suggesting an interaction between the radio and optical plasma in this region (C. S. Crawford & C. Vanderriest 2000). The source also shows associated absorption of C IV, N V, Si IV, and Ly $\alpha$  possibly due to the group of galaxies that this quasar lies in, with galaxies within 60 kpc of the quasar at the same redshift (J. E. Gunn 1971; J. N. Bahcall et al. 1993; E. Ellingson et al. 1994). It has a large (tens of kiloparsecs) irregular disturbed gas velocity field (over several hundred km s<sup>-1</sup>; J. B. Hutchings & D. Crampton 1990). The AGN resides in a 10'' undisturbed round host galaxy with an  $R^{1/4}$  luminosity profile (J. B. Hutchings & S. G. Neff 1992; Y. Zhao et al. 2021). The undisturbed nature of the host galaxy, the smooth optical profile, and the large size of the radio structure suggest that any AGN-triggering nuclear activity happened long ago given the typical major merger periods of 10<sup>8</sup>–10<sup>9</sup> yr (J. M. Lotz et al. 2011). The source is moderately weak in the soft X-ray band (W. N. Brandt et al. 2000).

### B.7. PG 2308+098

PG 2308+098 has an elliptical host galaxy with faint emission filaments extending to two nearby galaxies lying  $\sim 10''$  to the northeast and northwest (T. Gehren et al. 1984). It also has a weak associated absorber at  $z = 0.434$  (J. Bechtold et al. 2002). The optical–near-infrared spectral index of the polarized flux spectrum of PG 2308+098 suggests that the disk temperature profile of PG 2308+098 is consistent with the standard thin-disk model (M. Kishimoto et al. 2008).

### ORCID iDs

Janhavi Baghel  <https://orcid.org/0000-0002-0367-812X>  
P. Kharb  <https://orcid.org/0000-0003-3203-1613>  
T. Hovatta  <https://orcid.org/0000-0002-2024-8199>  
Luis C. Ho  <https://orcid.org/0000-0001-6947-5846>  
C. Harrison  <https://orcid.org/0000-0001-8618-4223>  
Silpa S.  <https://orcid.org/0000-0003-0667-7074>  
S. Gulati  <https://orcid.org/0000-0003-3785-1725>

### References

- Abdo, A. A., Ackermann, M., Agudo, I., et al. 2010, *ApJ*, **716**, 30  
Abdollahi, S., Acero, F., Baldini, L., et al. 2022, *ApJS*, **260**, 53  
Ajello, M., Baldini, L., Ballet, J., et al. 2022, *ApJS*, **263**, 24  
Akiyama, M., Ueda, Y., Ohta, K., Takahashi, T., & Yamada, T. 2003, *ApJS*, **148**, 275  
Angelakis, E., Hovatta, T., Blinov, D., et al. 2016, *MNRAS*, **463**, 3365  
Astropy Collaboration, Price-Whelan, A. M., Sipőcz, B. M., et al. 2018, *AJ*, **156**, 123  
Astropy Collaboration, Robitaille, T. P., Tollerud, E. J., et al. 2013, *A&A*, **558**, A33  
Baghel, J., Kharb, P., Hovatta, T., et al. 2024, *MNRAS*, **527**, 672  
Baghel, J., Kharb, P., Silpa, Ho, L. C., & Harrison, C. M. 2023, *MNRAS*, **519**, 2773  
Bahcall, J. N., Bergeron, J., Boksenberg, A., et al. 1993, *ApJS*, **87**, 1  
Bahcall, J. N., Kirhakos, S., Saxe, D. H., & Schneider, D. P. 1997, *ApJ*, **479**, 642  
Bahcall, J. N., Kirhakos, S., & Schneider, D. P. 1995, *ApJ*, **450**, 486  
Bardeen, J. M. 1970, *Natur*, **226**, 64  
Barthel, P. D. 1989, *ApJ*, **336**, 606  
Baum, S. A., Zirbel, E. L., & O'Dea, C. P. 1995, *ApJ*, **451**, 88  
Bechtold, J., Dobrzycki, A., Wilden, B., et al. 2002, *ApJS*, **140**, 143  
Begelman, M. C., & Silk, J. 2023, *MNRAS*, **526**, L94  
Bergeron, J., & Durret, F. 1987, *A&A*, **184**, 93  
Best, P. N., & Heckman, T. M. 2012, *MNRAS*, **421**, 1569  
Bicknell, G. V. 1984, *ApJ*, **286**, 68  
Bicknell, G. V. 1994, *ApJ*, **422**, 542  
Biretta, J. A., Zhou, F., & Owen, F. N. 1995, *ApJ*, **447**, 582  
Blackman, E. G., & Lebedev, S. V. 2022, *NewAR*, **95**, 101661  
Blandford, R. D., & Payne, D. G. 1982, *MNRAS*, **199**, 883  
Blandford, R. D., & Rees, M. J. 1974, *MNRAS*, **169**, 395  
Blandford, R. D., & Znajek, R. L. 1977, *MNRAS*, **179**, 433  
Block, D. L., & Stockton, A. 1991, *AJ*, **102**, 1928  
Blundell, K. M., & Rawlings, S. 2000, *AJ*, **119**, 1111  
Bogers, W. J., Hes, R., Barthel, P. D., & Zensus, J. A. 1994, *A&AS*, **105**, 91  
Boroson, T. A., & Green, R. F. 1992, *ApJS*, **80**, 109  
Boroson, T. A., & Oke, J. B. 1984, *ApJ*, **281**, 535  
Brandt, W. N., Laor, A., & Wills, B. J. 2000, *ApJ*, **528**, 637  
Bridle, A. H., & Perley, R. A. 1984, *ARA&A*, **22**, 319  
Cattaneo, A., Faber, S. M., Binney, J., et al. 2009, *Natur*, **460**, 213  
Cawthorne, T. V., & Hughes, P. A. 2013, *ApJ*, **771**, 60  
Cawthorne, T. V., Wardle, J. F. C., Roberts, D. H., & Gabuzda, D. C. 1993, *ApJ*, **416**, 519  
Chang, P., Broderick, A. E., & Pfrommer, C. 2012, *ApJ*, **752**, 23  
Clarke, D. A., Bridle, A. H., Burns, J. O., Perley, R. A., & Norman, M. L. 1992, *ApJ*, **385**, 173  
Crawford, C. S., & Vanderriest, C. 2000, *MNRAS*, **315**, 433  
Croston, J. H., Ineson, J., & Hardcastle, M. J. 2018, *MNRAS*, **476**, 1614  
Davis, S. W., & Laor, A. 2011, *ApJ*, **728**, 98  
Dennett-Thorpe, J., Bridle, A. H., Laing, R. A., & Scheuer, P. A. G. 1999, *MNRAS*, **304**, 271  
Ellingson, E., Yee, H. K. C., Bechtold, J., & Dobrzycki, A. 1994, *AJ*, **107**, 1219  
Falcke, H., Malkan, M. A., & Biermann, P. L. 1995, *A&A*, **298**, 375  
Fanaroff, B. L., & Riley, J. M. 1974, *MNRAS*, **167**, 31P  
Fender, R. P., Belloni, T. M., & Gallo, E. 2004, *MNRAS*, **355**, 1105  
Fossati, G., Maraschi, L., Celotti, A., Comastri, A., & Ghisellini, G. 1998, *MNRAS*, **299**, 433  
Gabuzda, D. C. 2003, *Ap&SS*, **288**, 39  
Gabuzda, D. C. 2015, in *Astrophysics and Space Science Library*, Vol. 414, The Formation and Disruption of Black Hole Jets, ed. I. Contopoulos, D. Gabuzda, & N. Kylafis (1; Springer Cham), 117978-3-319-10355-6  
Gabuzda, D. C., Cawthorne, T. V., Roberts, D. H., & Wardle, J. F. C. 1992, *ApJ*, **388**, 40  
Gabuzda, D. C., Pushkarev, A. B., & Cawthorne, T. V. 2000, *MNRAS*, **319**, 1109  
Gehren, T., Fried, J., Wehinger, P. A., & Wyckoff, S. 1984, *ApJ*, **278**, 11  
Ghisellini, G., Della Ceca, R., Volonteri, M., et al. 2010, *MNRAS*, **405**, 387  
Ghisellini, G., Padovani, P., Celotti, A., & Maraschi, L. 1993, *ApJ*, **407**, 65  
Ghisellini, G., Righi, C., Costamante, L., & Tavecchio, F. 2017, *MNRAS*, **469**, 255  
Ghosh, S., Kharb, P., Baghel, J., & Silpa, S. 2023, *ApJ*, **958**, 71  
Giommi, P., & Padovani, P. 1994, *MNRAS*, **268**, L51  
Giroletti, M., Giovannini, G., Taylor, G. B., & Falomo, R. 2006, *ApJ*, **646**, 801  
Godfrey, L. E. H., Lovell, J. E. J., Burke-Spolaor, S., et al. 2012, *ApJL*, **758**, L27  
Gopal-Krishna, Wiita, P. J., & Hooda, J. S. 1996, *A&A*, **316**, L13  
Gower, A. C., & Hutchings, J. B. 1984, *AJ*, **89**, 1658  
Grandi, P., Torresi, E., Macconi, D., Boccardi, B., & Capetti, A. 2021, *ApJ*, **911**, 17  
Green, R. F., Schmidt, M., & Liebert, J. 1986, *ApJS*, **61**, 305  
Gunn, J. E. 1971, *ApJL*, **164**, L113  
Hardcastle, M. 2018, *NatAs*, **2**, 273  
Hardcastle, M. J., Worrall, D. M., Kraft, R. P., et al. 2003, *ApJ*, **593**, 169  
Harwood, J. J., Hardcastle, M. J., Croston, J. H., & Goodger, J. L. 2013, *MNRAS*, **435**, 3353  
Harwood, J. J., Vernstrom, T., & Stroe, A. 2020, *MNRAS*, **491**, 803  
Hawley, J. F., Fendt, C., Hardcastle, M., Nokhrina, E., & Tchekhovskoy, A. 2015, *SSRv*, **191**, 441  
Hes, R., Barthel, P. D., & Fosbury, R. A. E. 1996, *A&A*, **313**, 423  
Ho, L. C., & Kim, M. 2015, *ApJ*, **809**, 123  
Hooper, E. J., Impey, C. D., Foltz, C. B., & Hewett, P. C. 1996, *ApJ*, **473**, 746  
Hutchings, J. B., & Crampton, D. 1990, *AJ*, **99**, 37  
Hutchings, J. B., Johnson, I., & Pyke, R. 1988, *ApJS*, **66**, 361  
Hutchings, J. B., & Neff, S. G. 1992, *AJ*, **104**, 1  
Intema, H. T., Jagannathan, P., Mooley, K. P., & Frail, D. A. 2017, *A&A*, **598**, A78  
Jang, M., & Miller, H. R. 1995, *ApJ*, **452**, 582  
Jester, S., Schneider, D. P., Richards, G. T., et al. 2005, *AJ*, **130**, 873  
Jurlin, N., Brienza, M., Morganti, R., et al. 2021, *A&A*, **653**, A110  
Jurlin, N., Morganti, R., Brienza, M., et al. 2020, *A&A*, **638**, A34  
Kapińska, A. D., Terentev, I., Wong, O. I., et al. 2017, *AJ*, **154**, 253

- Keenan, M., Meyer, E. T., Georganopoulos, M., Reddy, K., & French, O. J. 2021, *MNRAS*, **505**, 4726
- Kellermann, K. I., Lister, M. L., Homan, D. C., et al. 2004, *ApJ*, **609**, 539
- Kellermann, K. I., Sramek, R., Schmidt, M., Shaffer, D. B., & Green, R. 1989, *AJ*, **98**, 1195
- Kellermann, K. I., Sramek, R. A., Schmidt, M., Green, R. F., & Shaffer, D. B. 1994, *AJ*, **108**, 1163
- Kharb, P., Gabuzda, D., & Shastri, P. 2008a, *MNRAS*, **384**, 230
- Kharb, P., Gabuzda, D. C., O'Dea, C. P., Shastri, P., & Baum, S. A. 2009, *ApJ*, **694**, 1485
- Kharb, P., Lister, M. L., & Cooper, N. J. 2010, *ApJ*, **710**, 764
- Kharb, P., O'Dea, C. P., Baum, S. A., et al. 2008b, *ApJS*, **174**, 74
- Kharb, P., Stanley, E., Lister, M., et al. 2015, in *Extragalactic Jets from Every Angle*, Vol. 313 ed. F. Massaro, 211
- Kim, M., Ho, L. C., Peng, C. Y., Barth, A. J., & Im, M. 2017, *ApJS*, **232**, 21
- Kishimoto, M., Antonucci, R., Blaes, O., et al. 2008, *Natur*, **454**, 492
- Komissarov, S. S. 1994, *MNRAS*, **269**, 394
- Kylafis, N. D., Contopoulos, I., Kazanas, D., & Christodoulou, D. M. 2012, *A&A*, **538**, A5
- Laing, R. A. 1996, in *ASP Conf. Ser. 100, Energy Transport in Radio Galaxies and Quasars*, ed. P. E. Hardee, A. H. Bridle, & J. A. Zensus (San Francisco, CA: ASP), 241
- Laing, R. A., & Bridle, A. H. 2002, *MNRAS*, **336**, 328
- Laor, A. 2000, *ApJL*, **543**, L111
- Laor, A., Fiore, F., Elvis, M., Wilkes, B. J., & McDowell, J. C. 1997, *ApJ*, **477**, 93
- Lister, M. L., Aller, M., Aller, H., et al. 2013, *AJ*, **146**, 120
- Lister, M. L., & Homan, D. C. 2005, *AJ*, **130**, 1389
- Lister, M. L., Homan, D. C., Kellermann, K. I., et al. 2021, *ApJ*, **923**, 30
- Lotz, J. M., Jonsson, P., Cox, T. J., et al. 2011, *ApJ*, **742**, 103
- Luo, B., Brandt, W. N., Alexander, D. M., et al. 2013, *ApJ*, **772**, 153
- Lynden-Bell, D. 1969, *Natur*, **223**, 690
- Machalski, J., & Magdziarz, P. 1993, *A&A*, **267**, 363
- Mahatma, V. H. 2023, *Galax*, **11**, 74
- Márquez, I., Petitjean, P., Théodore, B., et al. 2001, *A&A*, **371**, 97
- Marscher, A., Jorstad, S., & Williamson, K. 2017, *Galax*, **5**, 63
- Massaro, F., Capetti, A., Paggi, A., et al. 2020, *ApJL*, **900**, L34
- McKean, J. P., Godfrey, L. E. H., Vegetti, S., et al. 2016, *MNRAS*, **463**, 3143
- McNamara, B. R., & Nulsen, P. E. J. 2007, *ARA&A*, **45**, 117
- Meier, D. L. 1999, *ApJ*, **522**, 753
- Meier, D. L., Koide, S., & Uchida, Y. 2001, *Sci*, **291**, 84
- Meyer, E. T., Fossati, G., Georganopoulos, M., & Lister, M. L. 2011, *ApJ*, **740**, 98
- Miller, P., Rawlings, S., & Saunders, R. 1993, *MNRAS*, **263**, 425
- Mingo, B., Croston, J. H., Best, P. N., et al. 2022, *MNRAS*, **511**, 3250
- Mingo, B., Croston, J. H., Hardcastle, M. J., et al. 2019, *MNRAS*, **488**, 2701
- Mullin, L. M., Riley, J. M., & Hardcastle, M. J. 2008, *MNRAS*, **390**, 595
- Neugebauer, G., Matthews, K., & Armus, L. 1995, *ApJL*, **455**, L123
- Oemler, Gunn, J. E., & Oke, J. B. 1972, *ApJL*, **176**, L47
- Olsen, E. T. 1970, *AJ*, **75**, 764
- Pacholczyk, A. G. 1970, *Radio Astrophysics*, cop. 1970
- Padovani, P., & Giommi, P. 2015, *MNRAS*, **446**, L41
- Paiano, S., Landoni, M., Falomo, R., et al. 2017, *ApJ*, **837**, 144
- Peacock, J. A. 1999, *Cosmological Physics* (Cambridge: Cambridge University Press) 9780511804533
- Perley, R. A., & Butler, B. J. 2017, *ApJS*, **230**, 7
- Pilkington, J. D. H., & Scott, J. F. 1965, *MmRAS*, **69**, 183
- Plavin, A. V., Kovalev, Y. Y., & Pushkarev, A. B. 2022, *ApJS*, **260**, 4
- Pooley, G. G., & Henbest, S. N. 1974, *MNRAS*, **169**, 477
- Pudritz, R. E., Hardcastle, M. J., & Gabuzda, D. C. 2012, *SSRv*, **169**, 27
- Punsly, B. 2011, *ApJL*, **728**, L17
- Punsly, B., Tramacere, A., Kharb, P., & Marziani, P. 2018, *ApJ*, **869**, 174
- Pushkarev, A. B., Aller, H. D., Aller, M. F., et al. 2023, *MNRAS*, **520**, 6053
- Rau, U., & Cornwell, T. J. 2011, *A&A*, **532**, A71
- Rawlings, S., & Saunders, R. 1991, *Natur*, **349**, 138
- Readhead, A. C. S., Cohen, M. H., Pearson, T. J., & Wilkinson, P. N. 1978, *Natur*, **276**, 768
- Rector, T. A., Stocke, J. T., & Ellingson, E. 1995, *AJ*, **110**, 1492
- Rees, M. J. 1966, *Natur*, **211**, 468
- Rees, M. J. 1984, *ARA&A*, **22**, 471
- Saikia, D. J., Salter, C. J., Neff, S. G., et al. 1987, *MNRAS*, **228**, 203
- Sambruna, R. M., Maraschi, L., & Urry, C. M. 1996, *ApJ*, **463**, 444
- Saripalli, L., Subrahmanyan, R., Thorat, K., et al. 2012, *ApJS*, **199**, 27
- Scheuer, P. A. G. 1974, *MNRAS*, **166**, 513
- Shangguan, J., Ho, L. C., & Xie, Y. 2018, *ApJ*, **854**, 158
- Shin, J., Woo, J.-H., Chung, A., et al. 2019, *ApJ*, **881**, 147
- Sikora, M. 2016, *Galax*, **4**, 12
- Sikora, M., & Begelman, M. C. 2013, *ApJL*, **764**, L24
- Sikora, M., & Zdziarski, A. A. 2023, *ApJL*, **954**, L30
- Silpa, S., Kharb, P., Harrison, C. M., et al. 2021a, *MNRAS*, **507**, 991
- Silpa, S., Kharb, P., O'Dea, C. P., et al. 2021b, *MNRAS*, **507**, 2550
- Simpson, C., Mulchaey, J. S., Wilson, A. S., Ward, M. J., & Alonso-Herrero, A. 1996, *ApJL*, **457**, L19
- Stalin, C. S., Gupta, A. C., Gopal-Krishna, A., Wiita, P. J., & Sagar, R. 2005, *MNRAS*, **356**, 607
- Stickel, M., Padovani, P., Urry, C. M., Fried, J. W., & Kuehr, H. 1991, *ApJ*, **374**, 431
- Stocke, J. T., Morris, S. L., Gioia, I. M., et al. 1991, *ApJS*, **76**, 813
- Stockton, A. 1978, *ApJ*, **223**, 747
- Stockton, A. 1982, *ApJ*, **257**, 33
- Stockton, A., & MacKenty, J. W. 1983, *Natur*, **305**, 678
- Stockton, A., & MacKenty, J. W. 1987, *ApJ*, **316**, 584
- Stockton, A., MacKenty, J. W., Hu, E. M., & Kim, T.-S. 2002, *ApJ*, **572**, 735
- Swarup, G., Saikia, D. J., Beltrametti, M., Sinha, R. P., & Salter, C. J. 1986, *MNRAS*, **220**, 1
- Tchekhovskoy, A. 2015, in *Astrophysics and Space Science Library*, Vol. 414, *The Formation and Disruption of Black Hole Jets*, ed. I. Contopoulos, D. Gabuzda, & N. Kylafis (Springer Cham), 45978-3-319-10355-6
- Urry, C. M., & Padovani, P. 1995, *PASP*, **107**, 803
- Vaddi, S., Kharb, P., Daly, R. A., et al. 2019, *MNRAS*, **484**, 385
- van Heerde, G. M. 1988, *A&A*, **201**, 213
- van Velzen, S., & Falcke, H. 2013, *A&A*, **557**, L7
- Veilleux, S., Rupke, D. S. N., Kim, D. C., et al. 2009, *ApJS*, **182**, 628
- Villafañá, L., Williams, P. R., Treu, T., et al. 2022, *ApJ*, **930**, 52
- Wang, A., An, T., Cheng, X., et al. 2023, *MNRAS*, **518**, 39
- Wardle, J. 2018, *Galax*, **6**, 5
- Wells, D. C. 1985, in *Data Analysis*, ed. V. di Gesu et al., 195 (Berlin: Springer)
- Whittam, I. H., Jarvis, M. J., Hale, C. L., et al. 2022, *MNRAS*, **516**, 245
- Wu, Z.-Z., Gu, M.-F., & Jiang, D.-R. 2009, *RAA*, **9**, 168
- Wykes, S., Hardcastle, M. J., Karakas, A. I., & Vink, J. S. 2015, *MNRAS*, **447**, 1001
- Wyndham, J. D. 1966, *ApJ*, **144**, 459
- Yates, M. G., Miller, L., & Peacock, J. A. 1989, *MNRAS*, **240**, 129
- Yee, H. K. C., & Ellingson, E. 1993, *ApJ*, **411**, 43
- Yee, H. K. C., & Green, R. F. 1984, *ApJ*, **280**, 79
- Yee, H. K. C., & Green, R. F. 1987, *ApJ*, **319**, 28
- Zhang, H., Li, X., Giannios, D., et al. 2020, *ApJ*, **901**, 149
- Zhao, Y., Ho, L. C., Shangguan, J., et al. 2021, *ApJ*, **911**, 94
- Zwicky, F., & Zwicky, M. A. 1971, *Catalogue of Selected Compact Galaxies and of Post-eruptive Galaxies*, (F. Zwicky, CH 3073 Guemligen(BE), Switzerland, 1971)